André Filipe Pereira Fernandes

Bachelor Degree in Sciences of Physics Engineering

Development of a code for highly charged ion plasma diagnostics through x-ray spectroscopy for astrophysical and energy applications

Dissertation submitted in partial fulfillment
of the requirements for the degree of

Master of Science in
Physics Engineering

Adviser: Prof. Dr. Mauro António Moreira Guerra,
NOVA University of Lisbon

Co-adviser: Prof. Dr. Miguel Ângelo Pignatelli de Avillez,
University of Évora,
Technical University of Berlin

Examination Committee

Chair: Prof. Dr. Maria Isabel Simões Catarino, NOVA University of Lisbon
Members: Prof. Dr. João Duarte Neves Cruz, NOVA University of Lisbon
Prof. Dr. Mauro António Moreira Guerra, NOVA University of Lisbon

FACULDADE DE
CIÊNCIAS E TECNOLOGIA
UNIVERSIDADE NOVA DE LISBOA

September, 2019

Development of a code for highly charged ion plasma diagnostics through x-ray spectroscopy for astrophysical and energy applications

This document was created using the (pdf)LaTeX processor, based on the "novathesis" template[1], developed at the Dep. Informática of FCT-NOVA [2].
[1] https://github.com/joaomlourenco/novathesis [2] http://www.di.fct.unl.pt

"A physicist is just an atom's way of looking at itself."
Niels Bohr

Acknowledgements

Em primeiro lugar quero agradecer ao meu orientador, Professor Doutor Mauro Guerra, pela disponibilidade e pelas tantas explicações, tornando possível a realização deste trabalho. Agradeço-lhe também por me ter inspirado interesse na investigação científica. Um obrigado ao meu coorientador, Professor Doutor Miguel Avillez, que me motivou a explorar e aprender sobre plataformas relevantes na área da astrofísica além do apresentado nesta tese. Finalmente, um obrigado a todos os professores da FCT NOVA que contribuíram para a minha aprendizagem ao longo deste curso.

Obrigado a todos os meus colegas que me acompanharam desde que entrei na faculdade, em especial o meu melhor amigo, Manuel Silva, que esteve sempre presente nos bons e maus momentos, que me fez rir e estudar, e que mudou profundamente a maneira como olho para o mundo. Muito obrigado por tudo Manuel. Obrigado à Catarina Sofia por conseguir perceber a minha tese e ajudar-me na realização das imagens com os seus desenhos.

Ik wil graag mijn professors en vrienden van de Universiteit Twente bedanken voor de rol die jullie hebben gespeeld tijdens mijn studie, in dit geweldige jaar. Graag wil ik Leonie, Sokje en alle anderen nog even apart bedanken. Jullie hebben mijn verblijf in Enschede compleet gemaakt en Nederland laten voelen als een thuis voor mij. Dankjewel voor alle Nederlandse lessen!

À minha família, não há palavras suficientes para agradecer. Mãe, pai, tenho muita sorte e orgulho em ter-vos como pais. Sem vocês esta etapa jamais seria concluída. Muito obrigado pelos sacrifícios que fizeram e por acreditarem em mim na concretização dos meus sonhos.

Abstract

Plasma diagnostics are crucial for projects like the International Thermonuclear Experimental Reactor (ITER), the world's largest tokamak, which is being built in the south of France. These diagnostics demand theoretical and experimental studies in order to understand the origin of spectral emissions observed in the plasma. From the balance between the creation and decay of excited states, one can infer on the ionic abundance within the plasma and hence on their quality. Thus, electron-impact ionization and excitation, which require cross section values for any creation process, need to be evaluated for a large number of states and for a wide energy range. Typically, the values are determined computationally with models such as the distorted wave Born approximation (DWBA) and, due to the simplicity of the approach and the large amount of atomic data needed for such codes, the modified relativistic binary encounter Bethe (MRBEB). With these, and the transition energies from the excited states, it is possible to determine the charge-state distribution within the plasma. With the ion structure information, we can determine, for example, the ion temperature and impurities from wall contamination in the plasma. The methodology is also relevant in the field of astrophysics, wherein theoretical calculations make it possible to know the characteristics of distant plasma bodies.

This work presents a code which can load x-ray experimental spectra and experimental transfer functions for irregular x-ray detection. The user can input several parameters and charge-state densities for the ions in order to present a simulated spectrum. A Levenberg-Marquardt algorithm was implemented in order to approximate the ion densities to the experimental data.

Keywords: Plasma diagnostics, x-ray quantification, highly charged ions, ITER, databases, cross sections, Levenberg-Marquardt

Resumo

O diagnóstico de plasmas é crucial para projetos como o *International Thermonuclear Experimental Reactor* (ITER), o maior *tokamak* do mundo, que está a ser construído no sul de França. Estes diagnósticos requerem estudos teóricos e experimentais para perceber a origem das emissões espetrais observadas no plasma. A partir do balanço entre a criação e o decaimento dos estados excitados, é possível inferir a abundância de iões dentro do plasma e assim a qualidade deste. Consequentemente, a ionização e a excitação por impacto eletrónico, que requerem valores das secções eficazes para a criação destes processos, necessitam de ser avaliadas para um grande número de estados e uma ampla gama de energias. Tipicamente, os valores são determinados computacionalmente com modelos como o *distorted wave Born approximation* (DWBA) e, devido à simplicidade da abordagem e da vasta quantidade de dados atómicos necessária para tais códigos, o *modified relativistic binary encounter Bethe* (MRBEB). Com estes, e as energias de transição a partir dos estados excitados, é possível determinar a distribuição dos estados de carga dentro do plasma. Com a informação da estrutura iónica, pode-se determinar, por exemplo, a temperatura dos iões e as impurezas devido a contaminações da parede no plasma. A metodologia é também relevante no campo da astrofísica, em que cálculos teóricos tornam possível saber as características de corpos de plasma distantes.

Este trabalho apresenta um código capaz de ler espetros experimentais de raios-x e funções de transferência experimentais para casos de deteção de raios-x não uniforme. O utilizador pode inserir vários parâmetros e valores da densidade de estados de carga dos diferentes iões, apresentando assim um espetro simulado. O algoritmo de Levenberg-Marquardt foi implementado para aproximar os valores de densidade dos estados de carga aos resultados experimentais.

Palavras-chave: Diagnóstico de plasmas, quantificação de raios-x, iões altamente carregados, ITER, bases de dados, secções eficazes, Levenberg-Marquardt

Contents

List of Figures

List of Tables

Listings

Acronyms

CPIPES	Collisional + Photo Ionization Plasma Emission Software
CSD	Charge-State Distribution
DCS	Double Crystal Spectrometer
DWBA	Distorted Wave Born Approximation
ECRIS	Electron-Cyclotron-Resonance Ion-Source
FAC	Flexible Atomic Code
FWHM	Full Width Half Maximum
GN	Gauss-Newton
GUI	Graphic User Interface
HCI	Highly Charged Ions
ITER	International Thermonuclear Experimental Reactor
LM	Levenberg-Marquardt
MCDF	Multiconfiguration Dirac-Fock
MCDFGME	Multiconfiguration Dirac-Fock and General Matrix Elements
MRBEB	Modified Relativistic Binary Encounter Bethe
PWBA	Plane Wave Born Approximation
SIMPA	Source d'Ions Multichargés de Paris

Chapter 1

Introduction

1.1 Motivation

Current energy resources offer a challenge for the years to come. With coal, oil and natural resources' limitation in conjunction with climate concerns, there is a demand for a clean, safe, and seemingly limitless source of energy. An ideal alternative to current sources is nuclear fusion which can generate great amounts of energy by fusing light atoms together with a positive energy output, analogous to how the sun works [1]. The cutting-edge nuclear fusion project is the International Thermonuclear Experimental Reactor (ITER) in France, based on a tokamak device. This design works with high temperature plasmas which are confined by intense magnetic fields and shielded by tungsten walls, being, as of date, the only practical method for nuclear fusion [2].

Plasma diagnostics is fundamental for this goal and requires a thorough theoretical study of a wide range of spectra, from x-rays to infrared. These spectra are analyzed by specific softwares, with spectral fitting packages such as Atomdb[1], Chianti[2], and XSPEC[3], in order to determine the origin and cause of the emissions observed in the plasma. These emissions stem from physical processes such as electron-impact excitation, electron-impact single and multiple ionization and, to a lower extent, photoionization and excitation. The softwares used have predetermined cross section values which demand a continuous update for a plasma diagnostic as close to reality as possible. The problem arises as there is no complete database from a single source for every electron-impact cross section, whether partial or total, of every element of interest in high temperature plasma physics. The data become even more scarce for ions with the atomic number $Z > 30$.

[1] atomdb.org
[2] chiantidatabase.org
[3] heasarc.gsfc.nasa.gov/xanadu/xspec

For fusion plasmas, due to their high temperatures and densities, it is crucial to have non-invasive methods for plasma diagnostics. This can be done by determining the ion Charge-State Distribution (CSD) from radiative emissions, causing no perturbation to the plasma [3]. Recently, it has been proven that it is possible to calculate the ion CSD of Highly Charged Ions (HCI) inside an Electron-Cyclotron-Resonance Ion-Source (ECRIS) plasma from high-resolution x-ray spectra [4]. The methodology based on considering the processes of excitation from electron-impact phenomena and decay within the plasma (processes of greatest influence in an ECRIS [5]). From there, for a given CSD, a theoretical spectrum is calculated. Once a CSD that best fits the experimental data is found, one can infer on the plasma composition, ergo, perform a diagnostic.

The aim of this master thesis is to develop a user friendly plasma diagnostics computer code, written in Python, that is able to gather databases for electron-impact excitation, single and multiple ionization for different atomic structures, determining the ion CSD. The user can change many parameters including the initial guess CSD and improve on them over experimental data with the Levenberg-Marquardt (LM) algorithm. The software is prepared to have an expandable database for a high number of ions with different atomic structures and intends on including the software Collisional + Photo Ionization Plasma Emission Software (CPIPES) [6] which other than considering electron-impact ionization, it also covers processes such as inner-shell excitation auto-ionization, radiative and dielectronic recombination to excited levels (followed by cascades), charge-exchange reactions, continuum (bremsstrahlung, free-bound and two-photon) and line (permitted, semi-forbidden, and forbidden) emission (see [7, 8]).

This work was presented at a poster session during the spring school and workshop EXSA Quantitative Methods in X-Ray Spectrometry in Portugal, May 2019.

1.2 State of the art

Inside ITER's plasma chamber, the thermonuclear fusions are based on either deuterium--deuterium or deuterium-tritium reactions. For these to have a positive energetic balance, the confined plasma must be in optimal conditions and the interaction with the tungsten walls minimal. Its hostile environment means any disruption in the plasma can significantly affect the fusion performance making it one of the main issues of the tokamak technology at ITER [9]. Therefore, plasma diagnostics work on actively controlling multiple parameters of the ion fluid and confirm plasma purity from possible wall contaminations, all the while providing the highest accuracy possible [10]. Although the plasmas are studied in every wavelength range, due to its high temperature, much of the radiated power is emitted in the x-ray range.

Spectra analysis on plasma emission can measure ion temperatures and toroidal rotation velocity, based on determinations of the Doppler broadening, centroid shift, and intensity of the lines of highly ionized impurities using a curved Bragg crystal spectral disperser and imager [11]. These studies are possible with high resolution spectrometers

like the Bragg x-ray crystal spectrometer KX1 built in the Joint European Torus (JET), one of the major tokamak ITER-like experiments. Upgrades to the crystals have been made where, in addition to helping inform on the nickel concentration, rotation velocity and ion temperature, the concentration of contaminating tungsten from ITER-like walls studies are possible [12]. This was done by having two measurement channels with each crystal for different orders of reflection, namely the "W channel" and "Ni channel". These were made to specifically measure the W^{46+} M-shell and Ni^{26+} K-shell lines respectively. The spectrometer was also built to avoid the detection of continuum emissions as they can interfere in identifying characteristic x-ray lines. The developed atomic models by Polasik [13, 14] based on Multiconfiguration Dirac-Fock (MCDF) calculations gave way to studies like Słabkowska *et al* (2014) [15] and Słabkowska *et al* (2015) [16]. These confirmed the possibility of a reliable x-ray analysis for the first time by modeling the spectra structures of M x-ray tungsten and L x-ray molybdenum emissions with the Flexible Atomic Code (FAC) package within the Collisional-Radiative (CR) model. Since this discovery, more modeling studies were performed for different x-ray lines for tungsten and molybdenum [17–19].

In 2017, the same plasma measurements were shown to be possible with the Core Imaging X-ray Spectrometer (CIXS) proposed for ITER plasmas, this time by studying the presence of W, Kr, Fe, Ar, and Xe in the plasma [20]. The diagnostics in the hot core are based on the L-shell W^{64+} or from K-shell Kr^{32+} lines by injecting Kr into the plasma. Analysis of the colder regions are given by the K-shell lines of Fe and Ar ions or alternatively by the Xe^{44+} L-shell line. Issues were raised as currently highly resolved x-ray spectroscopy depends on theoretical radiation models that consider all the relevant factors in order to identify tungsten's complex spectra, which is not yet fully understood. In fact, even for Ar ions, with electronic structures that are not very complex, the problem is not completely solved, as the number of important excitation and decay channels can be very high. These diagnostics rely on a large amount of high-quality atomic data of the excitation, ionization, and recombination rate coefficients as well as ionization balance calculations obtained from exhaustive theoretical studies [17, 21]. This rigorous demand has not been met yet [22].

1.3 Objectives of this research

The goal of this work is to organize an expandable database and provide for a better understanding of plasma diagnostics for a number of applications such as ITER. This will be done by building a computer software that relies on atomic data and is computed as needed with simple analytical expressions. All of the electronic structure calculations are performed using a state of the art computer code that employs the MCDF method.

1.4 Structure of the thesis

This thesis is divided into five chapters. Chapter 2 introduces the theoretical background behind the developed code, starting by explaining the different phenomena considered for x-ray emission inside a plasma. Then, since the code was tested with an Ar x-ray spectrum of the ECRIS plasma at Source d'Ions Multichargés de Paris (SIMPA), a description of the instruments are given as it is relevant for the plasma diagnostics. In the last section, the process of determining the CSD is described. Chapter 3 contains the developed PlasmaFit's Graphic User Interface (GUI)'s, flowcharts and listings, providing a detailed explanation of its structure and how the main modules were programmed. Chapter 4 presents the experimental spectrum of the ECRIS plasma as well as an analysis with a theoretical spectrum optimized to fit the data, resulting in the final CSD. Lastly, chapter 5 summarizes the work done throughout this master thesis and subsequent prospects.

Chapter 2

Theoretical background

This chapter details the theory behind the determination of the ion CSD from HCI through x-ray spectroscopy. An introduction on x-ray emissions and non radiative decay is followed by the presentation of the instruments used to produce HCI and detect the x-ray emission analyzed in this thesis. Lastly, the procedure for plasma diagnostics is explained.

2.1 X-ray emission

X-ray radiation was discovered by Wilhelm Conrad Röntgen in 1895, at the University of Würzburg [23]. Typically, this electromagnetic radiation ranges from 0.01 to 10 nm in wavelength, approximately, 0.1 to 100 keV. Since then, x-rays have been the target of extensive studies as they brought relevancy to a vast scope of technologies and to the understanding of the universe (e.g. diffuse medium in galaxies, supernova remnants, pulsars, black holes, and clusters of galaxies, to name a few).

Henry Moseley discovered in 1913 that the x-ray radiation wavelength is characteristic to the element in which the process occurred [24]. This meant that it was possible to determine unknown samples from their spectral emission, giving way to a field of x-ray spectroscopy for qualitative and quantitative elemental analysis [25].

For characteristic x-ray emission to happen, the element must be set up in a way that leaves a vacancy in one of its inner shells. This unoccupied orbital may come from the interaction of the atom or ion with particles such as photons, ions, and electrons, with sufficient energy to remove an electron from its inner orbital. As elements tend to be in its lowest state possible, a higher level electron will occupy this vacant orbital, releasing energy in the process. It may happen that this energy is then released as a photon with a wavelength in the x-ray range, as seen in Fig. 2.1.

The energy released is given by the energy difference between the levels:

$$E_{photon} = |E_f - E_i| \tag{2.1}$$

This emission results in a well defined spectrum with lines that are characteristic to the element, given that they correspond specifically to the transition energy between two orbitals. With other possible processes in mind, other than x-ray emission, these lines are able to provide a qualitative and quantitative analysis on their emission origin.

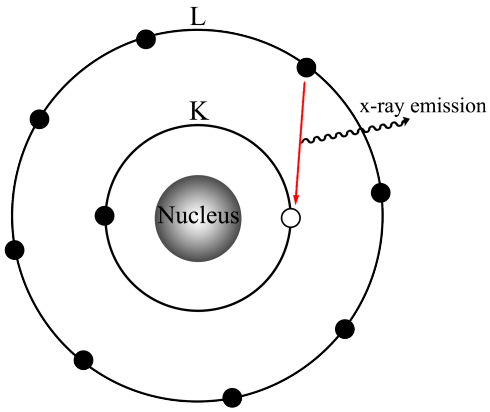

Figure 2.1: Schematic of x-ray emission where a higher level electron occupies a lower level shell.

2.1.1 Bremsstrahlung

As discussed earlier, interactions with the atom causing an unfilled orbital is required for characteristic x-ray emission. However, instead of causing a vacancy through excitation or ionization, the incident particle may decelerate and change its trajectory. Some energy is then converted into a continuous emission of x-ray photons. This process is called bremsstrahlung, German for "deceleration radiation".

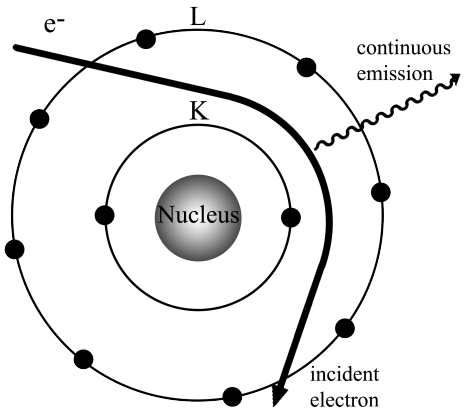

Figure 2.2: Schematic of electron-ion bremsstrahlung emission. As an electron interacts with the element, emitting a continuous x-ray radiation.

As the incident particle interacts with the nuclei Coulomb potential, its kinetic energy can be fully transferred into x-ray radiation, resulting in its maximum emission intensity. The particle can otherwise exit with some energy for another event. Consequently, there is a higher presence of bremsstrahlung in the lower end of the spectrum as lower energy events are more probable [26].

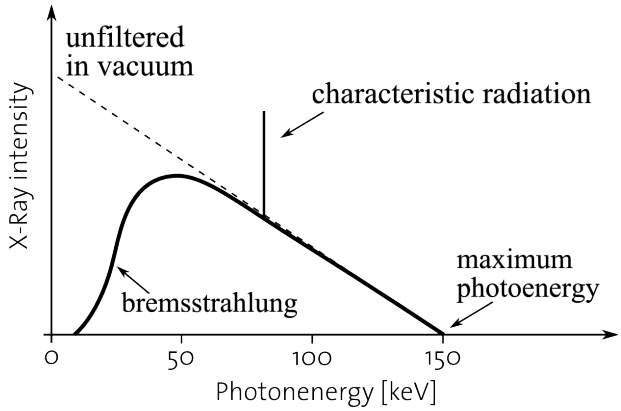

Figure 2.3: X-ray spectrum showing bremsstrahlung emission and a characteristic line. The dashed line is the unfiltered bremsstrahlung observed in a vacuum.

Fig. 2.3 shows a great decrease in x-ray intensity for lower energies, despite its increase down to 50 keV. This can be explained as low energy x-ray are difficult to detect since radiation is absorbed at really short distances through matter [27]. This absorption can occur either in the plasma itself (self-absorption) or by the presence of physical filters (Be entrance windows in the detectors, for example). For high energies ($\sim$ 300 keV), electron-electron bremsstrahlung starts to play a significant role in plasma emission (see Refs. [28, 29]). The phenomenon is similar to electron-ion bremsstrahlung, except the radiation wavelength depends on the angle between the direction of the emitting electron and the emitted photon. In astrophysics, it can happen that bremsstrahlung is the most important obtainable electromagnetic information, like in clusters of galaxies with plasma temperatures in the keV range, or group mergers that generate large-scale shock waves [30].

2.1.2 Auger electron emission

Alternatively to the event presented in Fig. 2.1, the Auger effect happens when the higher level electron occupies the lower level vacancy without the emission of radiation. As a consequence, the transition energy is transferred to another electron, causing its ejection. Despite this phenomenon being firstly discovered in 1923 by Lise Meitner, it was labeled after Pierre Auger in 1925 by independently discovering it once again [31].

Following the example in Fig. 2.4b, the upper level electron receives energy given by the difference between the $L_1 \rightarrow K$ transition. In case this energy is greater than the binding level energy corresponding to the $L_{2,3}$ orbital, the electron can be ejected from

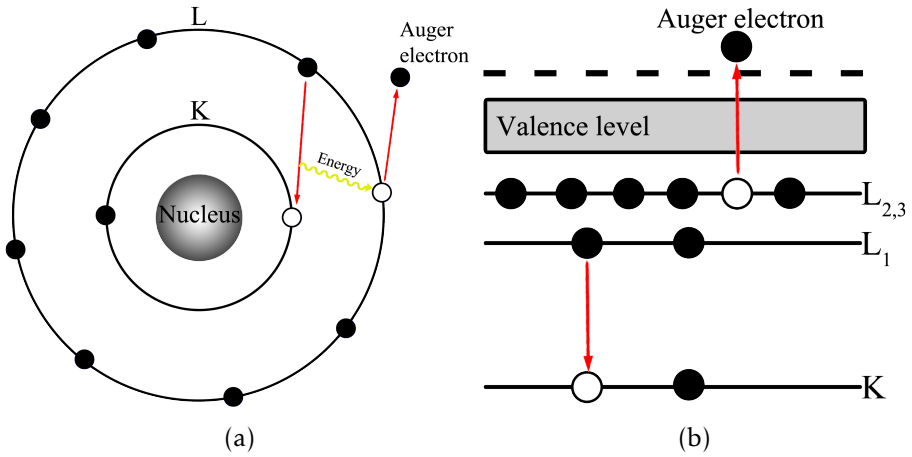

Figure 2.4: Schematic of an electron in the L-shell occupying a vacancy in the K-shell, transferring its transition energy to another electron, causing its emission (Auger electron).

the atom. Summarizing, the Auger electron will leave the atom or ion with the following energy:

$$E_{Auger} = |E_f - E_i| - E' \tag{2.2}$$

Where E_f and E_i are the energies of the final and initial state respectively, and E' the binding energy of the level in which the Auger electron originated. A special case of Auger emission happens in case the vacancy is filled from an electron of a higher subshell from the same shell, where it is named Coster-Kronig emission.

For lower atomic number elements ($Z < 40$), the relative energy level differences are greater, meaning a higher energy transfer, thus, a higher probability of Auger decay [32]. Considering Auger electrons are not present in x-ray spectra, it is to expect that the detected radiation does not offer sufficient information for x-ray quantification. For this reason, it is important to know the ratio/probability of radiative decay contrary to Auger electron emission. This ratio is called fluorescence yield, ω.

2.2 Electron-cyclotron-resonance ion-source (ECRIS)

Due to the fact that we do not have easy access to raw spectra from fusion tokamaks nor to the experimental specifications such as transfer functions and efficiencies, this work will evaluate experimental data obtained in an ECRIS at SIMPA. By comparing the experimental results of the CSD at SIMPA versus the theoretical distribution obtained from the code, it makes it evident that the code is properly working and ready to use for different measurements.

An ECRIS is a plasma ion source used for the production of HCI beams for a variety of fields and applications such as high energy physics, ion traps, x-ray spectroscopy or the interaction between ions and matter. The ECRIS was first conceptualized by Geller *et al* (1969) [33], followed by Potsma *et al* (1970) [34], with the first operational ECRIS in

1971 by Geller and co-workers. Thereafter, the technology has been target of study and new improvements (see Refs. [35–39]).

The basic principles of an ECRIS are depicted in Fig. 2.5 (Beyer *et al* [40]). In the first stage, a reservoir of electrons are emitted through a polarization electrode and flow inside the second stage, a metallic vessel under a strong magnet field. This vessel works both as a multi-mode cavity and a plasma chamber. Here, resonant electron heating by microwave radiation feeds energy in order to ignite the cold plasma. The microwave field is fueled by a 2 KW klystron embedded through a single ridge wave guide on the plasma chamber (which must have dimensions larger than the microwave wavelength used). A step by step ionization process produces the HCI. The production of electron density, electron velocity and ion confinement time, $n_e v_e \tau_c$, should be maximized and the neutral density minimized for a proper ion distribution in the plasma. Neutral atoms are undesirable given that they may interact with ions and lower the ionic charge. The minimum ion confinement time to successfully produce HCI like Ar^{16+} is deemed to be 10 ms [41]. To achieve this, the ECRIS technology resorts to magnetic traps or bottles in a B_{min} structure seen in Fig. 2.5. This field presents an hexapole configuration and is achieved through permanent magnets at SIMPA. Notwithstanding, one can also produce the same result with normal coils or even superconducting coils [42–44].

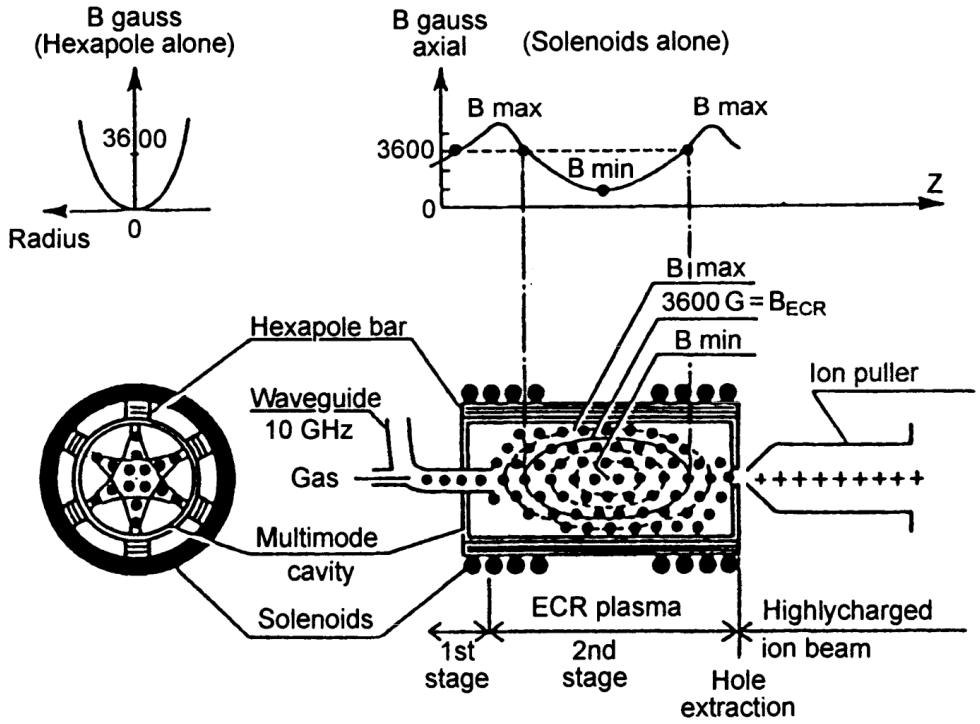

Figure 2.5: Principle of operation of a 10 GHz ECRIS. The plasma electrons are trapped in a B_{min} structure and are energized at the magnetic surface where the magnetic field is B_{ECR}. Image and caption taken from Ref. [40] ©1991 Springer.

As the temperature increases, high energy electrons prompt electron-impact excitation and ionization of the ions in their inner-shells. Consequentially, x-ray emissions are significant enough for plasma diagnostics [45]. In a commercial 14.5 GHz, all permanent magnets "supernanogan" types like at SIMPA, a few characteristics can be measured. Through bremsstrahlung spectra, one can deduce the electronic temperature [46] and with high-resolution x-ray spectroscopy it is possible to work out the CSD and electronic density [47].

Fig. 2.6 shows the type of ECRIS worked with at SIMPA. On the left side of the plasma chamber, a Double Crystal Spectrometer (DCS) detects the x-ray emission, advanced by the injection of gas and microwave radiation. The DCS and the pumping region are separated by a Be window resistant to vacuum pressure and is semi-transparent to low energy x-ray radiation, halving the intensity at low energies (~3 keV).

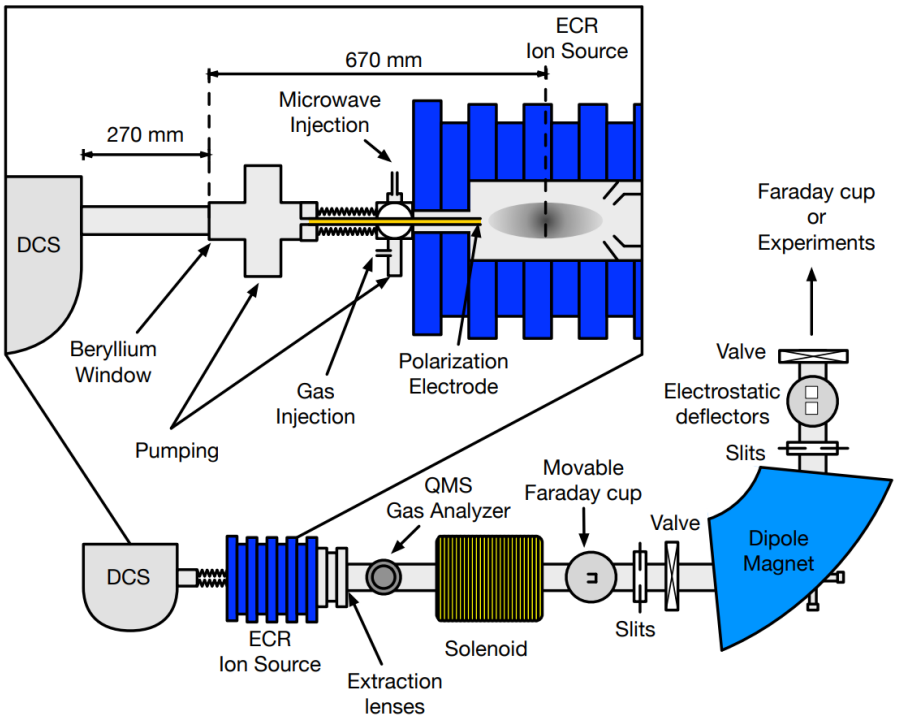

Figure 2.6: Representation of the ECRIS at SIMPA. The DCS on the left side detects x-rays from the center of the plasma after its ignition. On the right side of the ECRIS vessel, a system of extraction focuses and directs HCI for other studies such as electrostatic traps and surface interactions.

Other than plasma diagnostics from the DCS, spectroscopy inside an electrostatic trap, surface interaction with HCI or ECRIS' stability can be studied from the extraction of plasma on the right-hand side of the metallic vessel. As plasma exits through the electrostatic lenses, it is focused by a solenoid. Based on the dipole magnet current intensity, the HCI can be selectively sent to a faraday cup or elsewhere for a variety of experiments.

2.3 Double crystal spectrometer (DCS)

A DCS exploits Bragg's law in order to provide an x-ray spectrum. From Fig. 2.7, it is possible to see that as an x ray hits the first and second Si crystal, its path differs from the optical axis line (shown as dotted red). This is because of the connection between the wavelength λ of a certain ray and the reflection angle θ_B off the crystal's surface. The relation is given by the Bragg's law

$$n\lambda = 2d \sin\theta_B \tag{2.3}$$

Where n is the order of diffraction and d is the interplanar distance of the crystal.

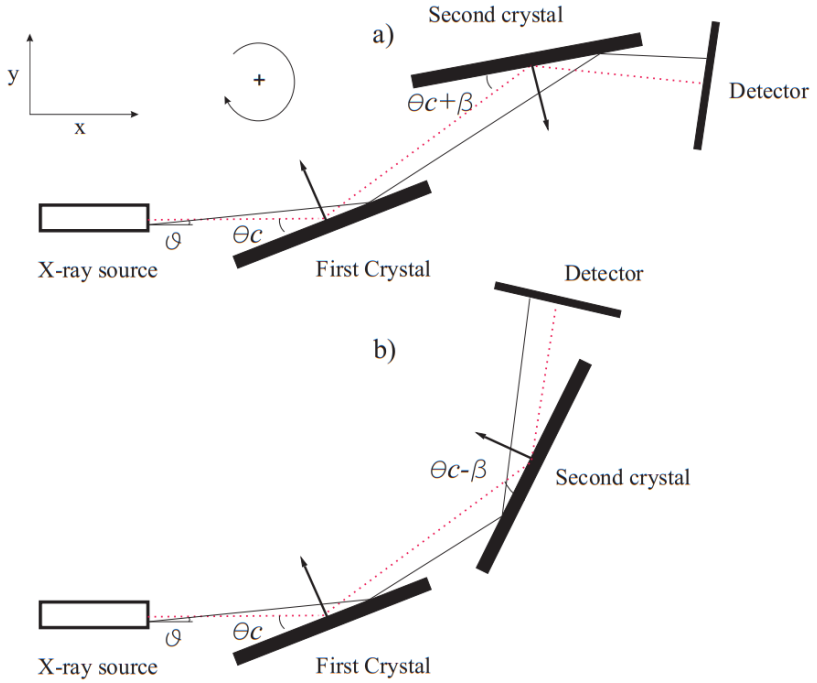

Figure 2.7: Scheme of the DCS in the horizontal plane. The reflections from the crystals can be set in a parallel (non-dispersive mode) or antiparallel (dispersive mode) manner represented in a) and b) respectively.

Alongside the polarization electrode by the plasma chamber, the first crystal will also work as a collimator for the rays reaching the second crystal. For a fixed angle of the first crystal, there are two arrangements for the second one to follow Bragg's law behavior: a parallel alignment (Fig. 2.7a) and an antiparallel one (Fig. 2.7b). With this, the *modus operandi* is as follows: while keeping the first crystal's angle static, the second crystal is rotated in parallel mode until the first peak is detected, then the same is done for the second peak in antiparallel mode. With both angles registered, one can calculate the Bragg's angle from

$$\theta_B = \frac{180 - (\theta_{disp} - \theta_{non-disp})}{2} \tag{2.4}$$

Where θ_{disp} and $\theta_{non-disp}$ are the dispersive and non-dispersive angle modes respectively.

At SIMPA, the DCS presents a peculiar configuration compared to other similar spectrometers. Most DCS have their crystals fixed with the x-ray source moving around pointed at the first crystal. As shown in Fig. 2.8, SIMPA's DCS has both crystal axis mounted in an optical table which rotates around the first crystal's axis. The crystal's angles are measured with encoders. The reason behind the static x-ray source at SIMPA is due to the large dimension and complexity of the vacuum system (see Fig. 2.9).

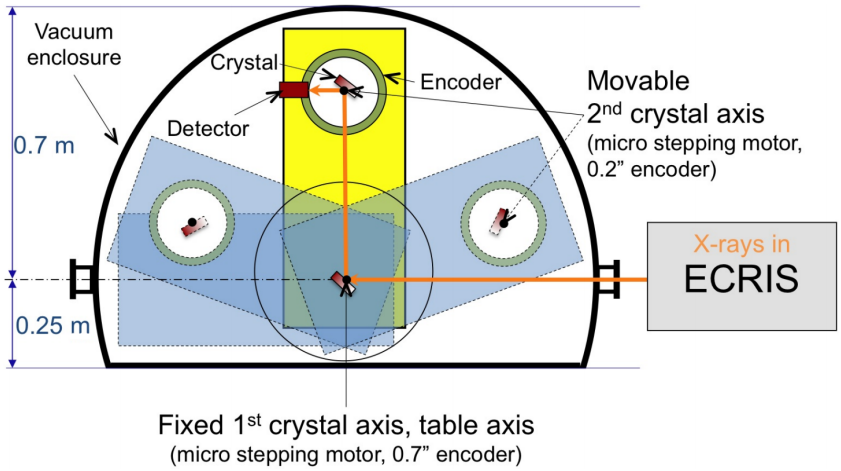

Figure 2.8: Top view of the DCS at SIMPA. Both crystals are placed in a single table with the second crystal rotating axis concentric with the first one. Next to the second crystal, the detector is placed which is able to rotate around the second crystal.

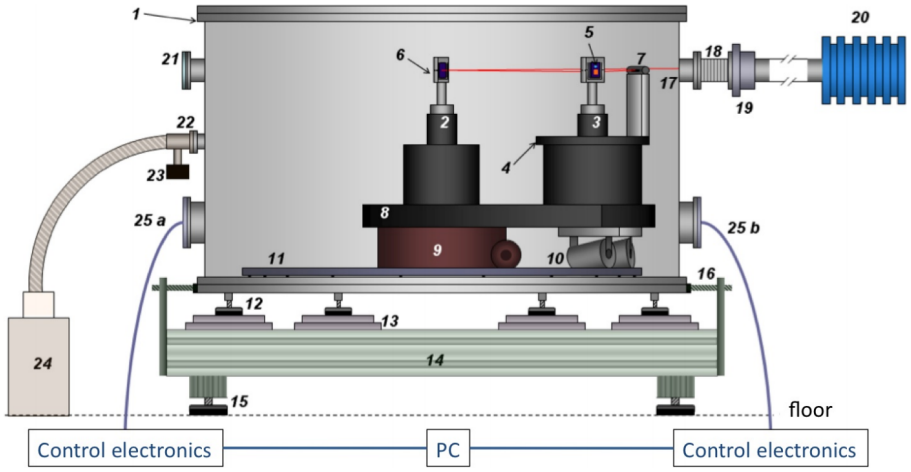

Figure 2.9: Schematic of the spectrometer setup. 1) vacuum enclosure; 2) axis #1 (crystal 1 and table); 3) axis #2 (crystal 2 and detector); 4) detector rotation support; 5) crystal; 6) crystal holder; 7) detector; 8) table; 9) table rotation support; 10) rotating cones; 11) tracks for cones; 12) enclosure support; 13) translation stages; 14) support; 15) legs; 16) translating screws; 17) x-ray entrance; 18) bellows; 19) Be window; 20) ECRIS SIMPA; 21) window; 22) connection to pumping; 23) pressure gauge; 24) rotary vacuum pump; 25) a and b feed-through for cables. Figure obtained from Ref. [48].

2.3.1 Detection intensity distribution

For plasma diagnostics, it can happen that a transfer function is associated with the final x-ray spectrum either due to geometrical constraints, the presence of filters, collimators, and so on, or due to the efficiency curves of elements within the optical path of the x--rays. Regarding the ECRIS explained in Sec. 2.2, there is a low energy attenuation as the rays travel through the Be window. In addition, Amaro (2011) [48] showed that, for a DCS, the ray distribution from the x-ray source depends on the shape of the geometrical slits and the distribution of the intensity of the focal spot. The histogram in Fig. 2.10 (Ref. [48]) shows the number of x-rays with uniform wavelength distribution hitting the first crystal as a function of the horizontal and vertical angles. It is noticeable that after the contribution of all collimators, the figure presents a cone-shape distribution function. The change in the first crystal's angle is related to the wavelength (energy; see Eq. 2.3), meaning the histogram shows a linear reduction in x-ray intensity from its peak with the variation of energy. Furthermore, the vertical angle φ does not change with the horizontal angle θ. Hence, it is to expect a transfer function (on φ) with either a triangular or hyperbolic distribution. The difference will come down to the vertical divergence value being either approximately zero or not, respectively.

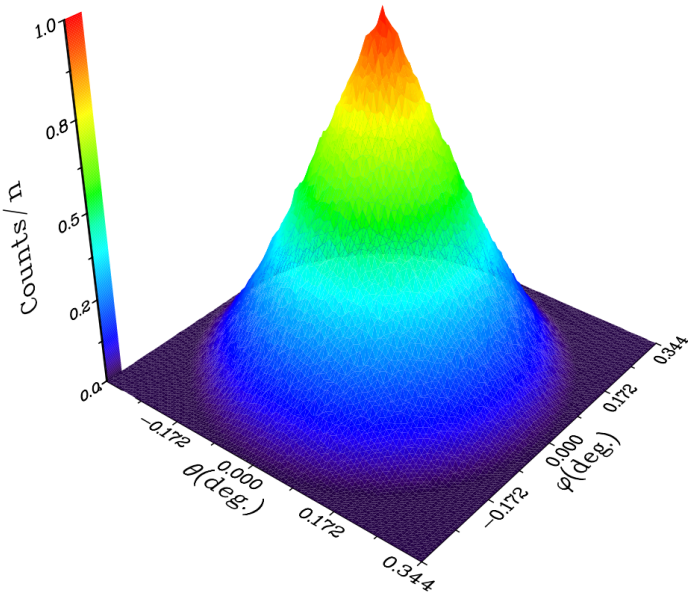

Figure 2.10: Histogram of the number of rays for values of φ and θ (horizontal and vertical angles, respectively). The rays presented a uniform focal distribution with a cylindrical shape alignment. From Amaro (2011) [48].

Fig. 2.11 shows the simulated maximum number of rays reaching the detector as a function of the energy, over a triangular and a hyperbolic fit obtained from Guerra *et al* [4] (see normalized Eqs. 2.5 and 2.6). We can see that the vertical divergence is not really zero, indicating that a hyperbolic fit might be more appropriate. The reason the tails diverge from either hyperbolic or triangular distribution is because the x-rays start

to hit the edge of the second crystal of the DCS where dynamical effects may occur and influence the intensity.

$$I_{triangular}(E) = 16611.5 - |826.462 \times E - 2565220| \tag{2.5}$$

$$I_{hyperbolic}(E) = 1.04815 - 6.27647 \times 10^{-5} \times \sqrt{|588509 + 690026(E - 3103.89)^2|} \tag{2.6}$$

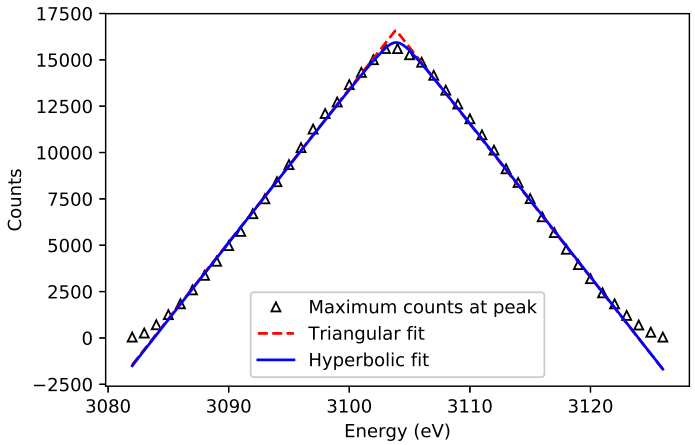

Figure 2.11: Intensity distribution of the x-rays reaching the DCS. The triangular fit is represented by the red dashed line and the hyperbolic fit the blue line (Eqs. 2.5 and 2.6 respectively).

2.4 Plasma diagnostics

For a proper x-ray spectrum analysis of ECRIS plasma, with the aim of estimating the ion CSD, one must take into consideration the physical processes in it. The methodology for the CSD estimation is as follows (Santos *et al* [49]):

1. The spectrum of characteristic x-rays from ions inside the plasma is measured;
2. The excited states that produce the x-ray spectrum are identified through extensive atomic databases;
3. The main processes leading to these excited states, from the ground configurations, are found and the corresponding cross sections are calculated, using a physically justified electron distribution function;
4. Radiative and radiationless transition energies and probabilities are calculated (or extracted from a database) for the identified excited states;
5. From the comparison of the peak intensities in theoretical and experimental spectra, the CSD is obtained iteratively followed by the application of a LM algorithm, designed for non-linear optimization and curve fitting problems;

This work takes into account the transition energies and radiative probabilities, the distribution of electron energies in the plasma and electron-impact excitation, single, double and triple ionization. For an ECRIS, the electron-impact phenomena are of greatest influence to the spectrum [5]. Notwithstanding, other processes can occur, such as dielectronic recombination, charge exchange, two-photon emission, and radiative recombination. The decay processes considered are either characteristic x-ray emission or radiationless transition. The plasma is considered to be in population equilibrium, since it is constantly fueled by the microwave radiation. On point 5, with a balance equation, it is possible to relate the line intensities with the CSD explained on section 2.4.5.

2.4.1 Electron-impact excitation

Electron-impact excitation is the interaction of an incident electron with an element, resulting in the transition of an electron to a higher level orbital (Fig. 2.12).

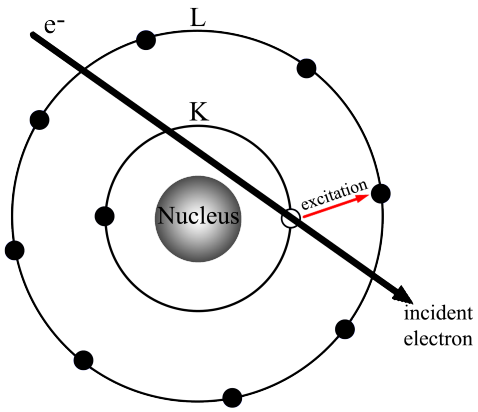

Figure 2.12: Schematic of electron-impact K-shell excitation. An incident electron interacts with the atom causing the excitation of one of the K-shell electrons towards another shell.

Plasma phenomena interpretation from electron-impact excitation can be done from atomic database cross section values (see [50, 51]). In these databases, many cross section values have been either calculated or determined experimentally, however, there are many values missing for specific ions or energy intervals. Fisher *et al* [52], based on the van Regemorter expression for bound-bound electron excitation [53] have been able to estimate electron-impact excitation cross sections. This expression presents a flaw in which it considers only electric dipole transitions, insufficient for ions. A proper attempt is to calculate through computer codes such as the Multiconfiguration Dirac-Fock and General Matrix Elements (MCDFGME) of Desclaux and Indelicato [54–56]. This code not only determines excitation cross section values but also the transition energies and radiative and radiationless transition probabilities. The code resorts to the first Born approximation for electron and photon impact cross sections, with MCDF wave functions for the atom and a Dirac wave function for the free electron [57].

For high energies, where the electron interaction is minimal, this is a sufficient approach to get an accurate calculation, but for lower energies, meaning a higher electron interaction, the electron-impact excitation cross sections should be computed using the Distorted Wave Born Approximation (DWBA) [15, 18]. DWBA, an extension of the Plane Wave Born Approximation (PWBA), accounts for higher-order multiple scattering effects. Now, the electron-electron interaction of the projectile and target is no longer considered negligible [58]. While it is more demanding in computational terms, it provides better results as seen in Fig. 2.13 [59].

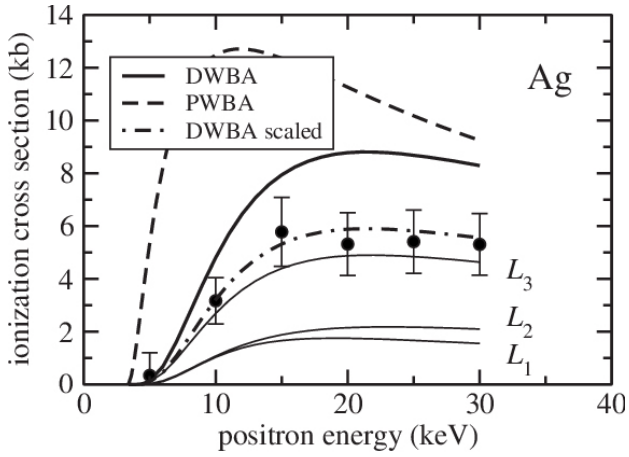

Figure 2.13: Cross section for the ionization of the L-shells of Ag by positrons over their energy. The solid and dashed curves represent the calculations performed with DWBA and PWBA, respectively. Partial DWBA cross sections for the L_1, L_2 and L_3 subshells are depicted as thin solid curves. The circular symbols represent the experimental data measured by Nagashima *et al* [60].

2.4.2 Electron-impact ionization

Electron-impact ionization is the interaction of an incident electron with an element resulting in the eviction of electrons (see Figs. 2.14 or 2.16).

2.4.2.1 Single ionization

When it comes to electron-impact ionization cross sections, there are some added computational challenges. Whether they are single, double or triple ionizations, many of the developed computational models take a substantial amount of time to compute [61, 62]. Despite their accuracy, these are limited to simple valence shell structures and light atoms. For plasmas with heavier atoms and many possible ionization pathways, a simpler model must be used to calculate the ionization cross sections. These models should be able to describe highly energetic electrons based on a quantum-mechanical description with a proper analysis of the asymptotic high energy behavior of the cross sections.

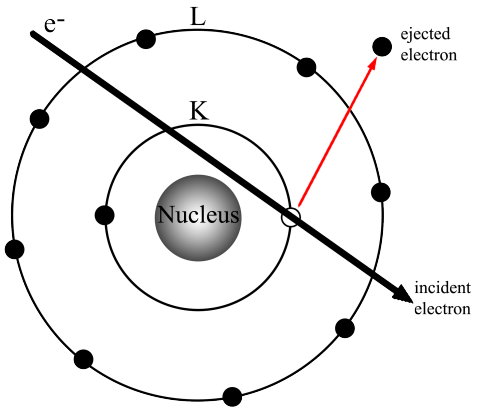

Figure 2.14: Schematic of electron-impact K-shell ionization. An incident electron interacts with the atom causing a single ionization in the K-shell.

Although it is possible to use methods such as DWBA, a simpler option would be to employ the Modified Relativistic Binary Encounter Bethe (MRBEB) method [63–65]. The MRBEB model is a product of a series of improvements, starting from the Mott description of two identical particles, to the Binary Encounter Dipole (BED) model, to the Binary Encounter Bethe (BEB) one. Recently, de Avillez *et al* (2019) [8] showed that the MRBEB provides cross section values with the same degree of quality as more complex alternatives like DWBA and FAC for carbon ions. The total ionization cross section of an $n\ l\ j$ bound electron (n being principal quantum number, l orbital angular momentum and j total angular momentum) with binding energy B in an atom in the initial state LS (L being the total orbital angular momentum and S the total spin angular momentum), by an electron with incident kinetic energy T reads

$$\begin{aligned}\sigma_{MRBEB,nljLS} = \frac{4\pi a_o^2 \alpha^4 N_{nlj}}{(\beta_t^2 + \chi_{nlj}\beta_b^2)2b'}\Bigg\{\frac{1}{2}\left[\ln\left(\frac{\beta_t^2}{1-\beta_t^2}\right) - \beta_t^2 - \ln(2b')\right]\times \\ \left(1-\frac{1}{t^2}\right) + 1 - \frac{1}{t} - \frac{\ln t}{t+1}\frac{1+2t'}{\left(1+\frac{t'}{2}\right)^2} + \frac{b'^2}{\left(1+\frac{t'}{2}\right)^2}\frac{t-1}{2}\Bigg\}\end{aligned} \tag{2.7}$$

With

$$\begin{aligned}\beta_t^2 &= 1 - \frac{1}{(1+t')^2};\ t' = \frac{T}{mc^2} \\ \beta_b^2 &= 1 - \frac{1}{(1+b')^2};\ b' = \frac{B}{mc^2} \\ t &= \frac{T}{B};\ \chi_{nlj} = \left(\frac{C_{nlj}}{B}\right)2R\end{aligned} \tag{2.8}$$

Where α is the fine structure constant, c is the speed of light in vacuum, m is the electron mass, R the Rydberg energy (13.6 eV), N_{nlj} is the subshell occupation number, a_o the Bohr radius (5.29×10^{-11} m) and C_{nlj} is the scaling factor given by

$$C_{nlj} = 0.3\frac{Z_{eff_{nlj}}^2}{2n^2} + 0.7\frac{Z_{eff_{n'l'j'}}^2}{2n'^2} \tag{2.9}$$

With $n'\ l'\ j'$ being the following subshell after the subshell $n\ l\ j$, ordered in ascending energy. The $Z_{eff_{nlj}}$ are obtained from Ref. [66]. The cross section comparison of Se and Kr between different models for electron-impact L-shell ionization is shown in Fig. 2.15.

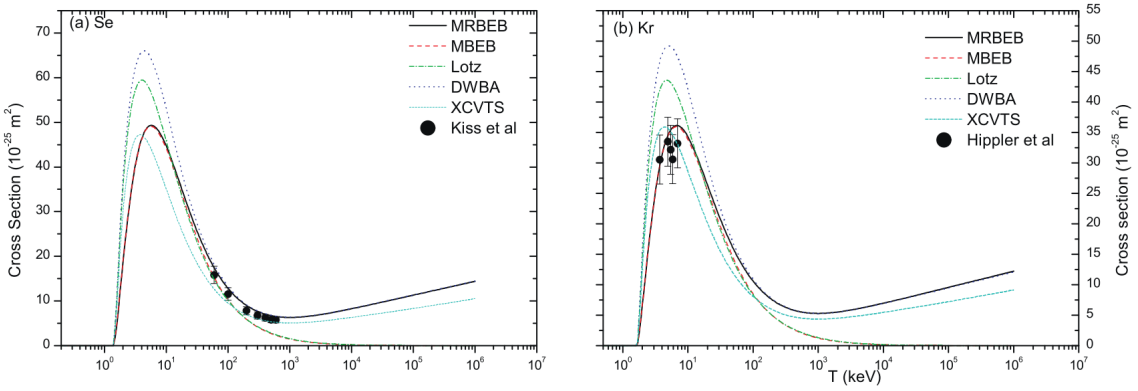

Figure 2.15: Electron-impact L-shell ionization cross section for (a) Se and (b) Kr. The thick solid curve represents the MRBEB cross section according to Eq. 2.7; dash-dash curve, Modified Binary Encounter Bethe (MBEB) cross section [66]; dot-dash curve, relativistic empirical formula by Lotz [67]; dot-dot curve, DWBA by Bote *et al* [68]; short dot-dash curve, XCVTS semiempirical formula by Haque *et al* [69]; the symbols are the experimental data for Se by Kiss *et al* [70] and for Kr by Hippler *et al* [71]. Graphs taken from [64].

2.4.2.2 Double and triple ionization

For electron-impact multiple ionization, the cross sections of the double-KL and triple--KLL ionization processes from the ground-state configuration are calculated by a semi--empirical formula of Shevelko and Tawara [72]. The cross section formula, developed for the purpose of the outermost electrons' ionization, is given as

$$\sigma_n = \frac{a(n)N^{b(n)}}{\left(\frac{I_n}{Ry}\right)^2}\left(\frac{u}{u+1}\right)^c \frac{\ln(u+1)}{u+1}10^{-18} \qquad [\text{cm}^2] \quad (2.10)$$

Where

$$u = \frac{E}{I_n} - 1 \quad (2.11)$$

With E being the incident electron energy in eV, I_n the ionization energy required to remove the KL, or KLL, electrons from the target, in eV, N the total number of target electrons, 1 Ry = 13.6 eV, and $c = 1$ for neutral atoms and $c = 0.75$ for ions. The fitting parameters $a(n)$ and $b(n)$ proposed by Bélenger *et al* [73] are $a(2) = 14.0$ and $b(2) = 1.08$ for double ionization, and $a(3) = 6.30$ and $b(3) = 1.20$ for triple ionization.

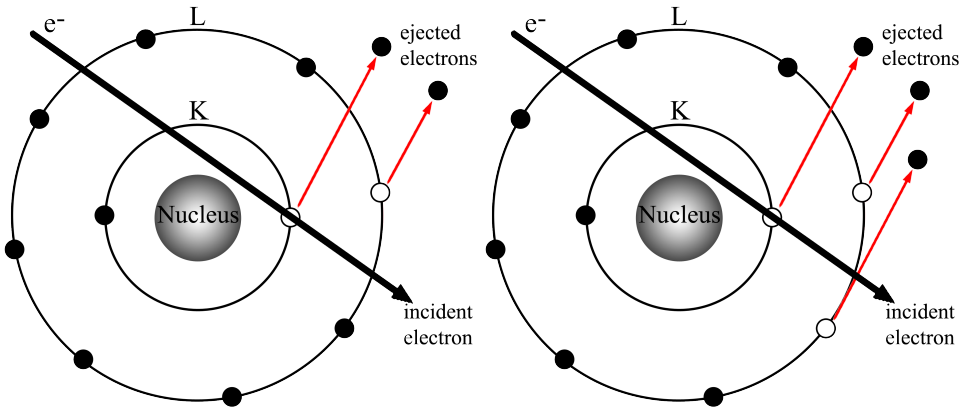

(a) K- and L-shell double ionization (b) K- and L-shell triple ionization

Figure 2.16: Schematic of electron-impact with multiple ionizations. An incident electron interacts with the atom causing electronic ionizations in the K- and L-shell.

2.4.3 Transition energies and probabilities

For an accurate analysis of x-ray spectra, the transition energy values, probabilities and fluorescence yields are crucial. There are some considerations which must be taken into account in order to calculate them. Firstly, for some electrons, the correlation distribution to transition energies is very important, meaning there is a need of a multiconfiguration or configuration-interaction approach. The MCDFGME approach is characterized by the fact that a small number of configurations can account for a large amount of correlation [74, 75]. Secondly, for HCI, the electrons demonstrate a strong relativistic behavior, implying consideration for relativistic effects. And finally, quantum-electrodynamics effects such as the electron's self-energy and vacuum polarization must be added.

2.4.4 Distribution of electron energies in the plasma

It may happen in plasmas that the electron distribution is strongly non-Maxwellian and is divided into two populations, a low energy cold population, and a hot one with significantly higher energies. In an ECRIS, the hot population can be well confined inside a closed egg-shaped surface centered around the source main axis, being considered a non-Maxwellian distribution. The cold population electron distribution, on the other hand, is approximately Maxwellian [46, 76]. As seen in Pras *et al* [77], the global electron distribution $f(E)$ can be represented as a linear combination of the Maxwellian and the non-Maxwellian electron distributions, $f_{Mw}(E)$ and $f_{NMw}(E)$ respectively.

The rate of the number of events of a certain process, whether by excitation or ionization, averaged over the electron distribution energy is given by

$$\langle N_e \, \sigma \, v \rangle = N_e \int_{E_{min}}^{\infty} v(E)\sigma(E)f(E)dE \tag{2.12}$$

With the global electron distribution defined as

$$f(E) = (1-x)f_{Mw}(E) + xf_{NMw}(E) \tag{2.13}$$

Where N_e is the electron density, $\sigma(E)$ the process' cross section, $v(E)$ the electron velocity, at an electron energy E and x is a mixing coefficient dependent on the plasma temperature.

The Maxwellian distribution $f_{Mw}(E)$ reads

$$f_{Mw} = \frac{2}{\sqrt{\pi}} \frac{E^{1/2}}{(kT_{cold})^{3/2}} e^{-E/kT_{cold}} \tag{2.14}$$

Where T is the temperature, k the Boltzmann constant and the velocity v in the relativistic form of E is given as

$$v = cE^{1/2} \frac{(E + 2mc^2)^{1/2}}{(E + mc^2)} \tag{2.15}$$

For the cold population, we resort to the Gauss-Laguerrer integration [78] for the calculation of the following integral. For now, this integration is used as it requires a small number of cross sections for each ion, process, and energy. Other more complex methods could be applied if these values are then to be provided on a large scale database.

$$\int_{E_{min}}^{\infty} f_{Mw}(E)v(E)\sigma(E)dE \tag{2.16}$$

Can be transformed into the form

$$\int_0^{\infty} g(x)e^{-x}dx \tag{2.17}$$

Through variable transformation and rearrangements, we have

$$\int_{E_{min}}^{\infty} f_{Mw}(E)v(E)\sigma(E)dE = \frac{2c}{\sqrt{\pi}} \frac{e^{-E_{min}/kT_{cold}}}{(kT_{cold})^{1/2}} \int_0^{\infty} g(x)e^{-x}dx \tag{2.18}$$

Where

$$g(x) = (xkT_{cold} + E_{min}) \frac{(xkT_{cold} + E_{min} + 2mc^2)^{1/2}}{xkT_{cold} + E_{min} + mc^2} \sigma(xkT_{cold} + E_{min}) \tag{2.19}$$

For the hot population with the non-Maxwellian distribution $f_{NMw}(E)$, it reads

$$f_{NMw}(E) = C_n E \left(1 + \frac{E}{2mc^2}\right)\left(1 + \frac{E}{mc^2}\right) e^{-E/kT_{hot}} \tag{2.20}$$

And

$$C_n = \frac{1}{(kT_{hot})^2} \frac{1}{1 + 3\alpha + 3\alpha^2};\ \alpha = \frac{kT_{hot}}{mc^2} \tag{2.21}$$

Through the same integral arrangements, we have

$$\int_{E_{min}}^{\infty} f_{NMw}(E)v(E)\sigma(E)dE = \frac{C_n ckT_{hot}}{2(mc^2)^2} e^{-E_{min}/kT_{hot}} \int_0^{\infty} g(x)e^{-x}dx \tag{2.22}$$

Where

$$g(x) = (xkT_{hot} + E_{min})^{3/2}(xkT_{hot} + E_{min} + 2mc^2)^{3/2}\sigma(xkT_{hot} + E_{min}) \tag{2.23}$$

Note that some works have used the mixing coefficient of $x = 0.99$, meaning an almost Maxwellian distribution inside hot population plasma, and has provided reliable experimental results [49, 79]. Still, for high temperature plasmas, it is still not clear what the correct mixing coefficient should be.

2.4.5 Balance equation

As a final step, the balance equation helps determine the line intensities. From Fig. 2.17, the left column being the initial states, the middle column the excited states and the right column the following decay states, one can take a few simple ideas. The understanding from this work comes down to ionic population, supply of excited states and their radiative decay potential. In an x-ray plasma spectrum, one would expect the states with higher radiative decay probability to present greater intensities, yet the supply of the excited states responsible for those likely transitions may be lower and show smaller peaks. Moreover, the population of the ions from the initial states also interfere with the experimental results.

The transition energies considered are from excited states with specific LSJ terms, however, the electron-impact phenomena may end with different magnetic quantum numbers. This means that the probability of a certain phenomena resulting in the excited state must be calculated. The calculation is as follows

$$sp = \frac{2j_f + 1}{\sum 2j_f + 1} \tag{2.24}$$

With sp being the probability of the excited state ending up in the $2j + 1$ states of interest over the sum of all the possible states. Since the stored cross section values for electron-impact K-shell excitation always express the final LSJ configuration, the probability will be 1 as long as it matches with the terms of the transitions energies.

In this work, all ions are considered to be in the ground state initially[1], with charge state q. This is because, for Ar HCI in an ECRIS, the lifetime of the excited states are orders of magnitude lower than the collision times for the considered processes (10^6 s^{-1} and 10^9-10^{15} s^{-1}, respectively) [80]. The charge state is defined as the degree of ionization with $q = Z - m$, where m is the number of bound electrons in the ion. With a process of an ion in the charge state q and K hole in the excited level i, the balance equation is

$$\begin{aligned} N_0^q\langle N_e v\sigma_i^{K-exc,q}\rangle + N_0^{q-1}\langle N_e v\sigma_i^{K-ion,(q-1,q)}\rangle + N_0^{q-2}\langle N_e v\sigma_i^{KL-ion,(q-2,q)}\rangle + \\ + N_0^{q-3}\langle N_e v\sigma_i^{KLL-ion,(q-3,q)}\rangle = N_i^{K,q}A_i^q \end{aligned} \tag{2.25}$$

Where A_i^q is the radiative or radiationless decay probability at the level i and $N_0^{q'}$ the q' charge-state ion density in the ground configuration. $\sigma_i^{K-exc,q}$ is the excitation cross

[1] A metastable state was added into the final database for a more accurate analysis.

section of the processes where an ion in the charge state q reaches the excited level i of the same ion with a K hole. This cross section represents the sum of all the cross sections for the processes from each level j to the excited level i, weighted by its probability. $\sigma_i^{K-ion,(q-1,q)}$, $\sigma_i^{KL-ion,(q-2,q)}$ and $\sigma_i^{KLL-ion,(q-3,q)}$ represent the single, double, and triple ionization cross sections respectively, of the processes where an ion of charge state q' $(q' = q-3, q-2, q-1, q)$ reaches the excited level i with charge q and a K hole. These are calculated from the MRBEB electron-impact single ionization cross section in Eq. 2.7 and the semi-empirical formula in Eq. 2.10. $N_i^{K,q}$ is the ion density in the charge state q in the ground state and a K-shell hole in the level i. Finally, $N_0^q \langle N_e v \sigma_i^{process} \rangle$ is the rate of the number of events related to the process in question. Certain adjustments to the balance equation will change the spectra simulations. It can be done by trial and error or by fitting using a LM algorithm and result in reliable values of the CSD inside the plasma. The line intensity of a certain ion $i \rightarrow j$ transition with charge q and K-shell hole can be calculated from the following equation

$$I_{ij}^q = \hbar\omega A_{ij}^q N_i^{K,q} \tag{2.26}$$

With $\hbar\omega$ being the transition energy, A_{ij}^q the radiative transition probability from level i to j. $N_i^{K,q}$ represents the ion density from the solved balance equation 2.25. Once the calculated intensity lines from 2.25 correspond with the experimental spectrum, the ion densities yield the CSD.

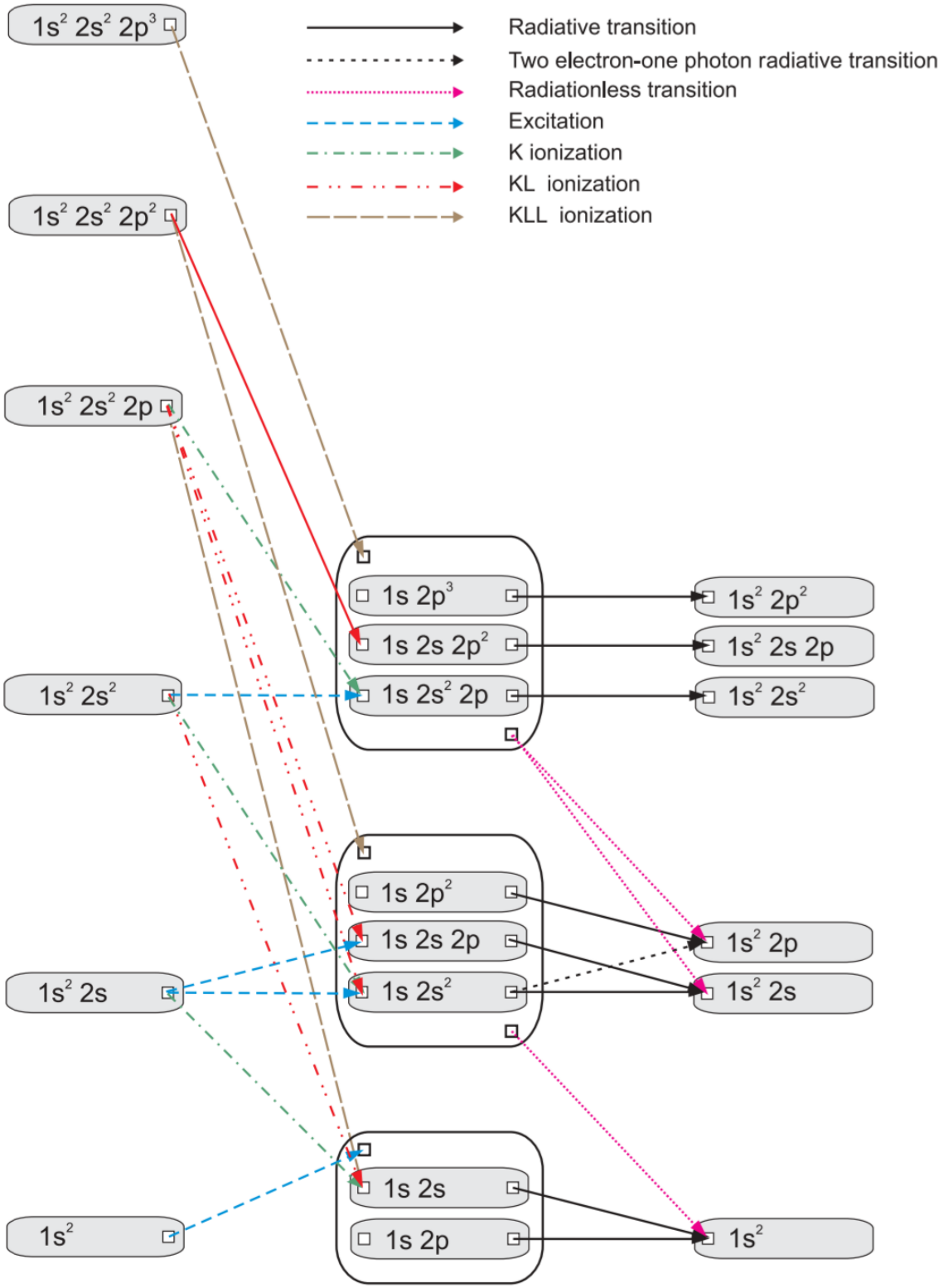

Figure 2.17: Sequence of excitation from ground states and decay under different processes considered by Santos *et al* [49]. The K excitation is represented by a dashed line; the single K ionization as a dot-dashed line; the KL double ionization as a dot-dot-dashed line; the KLL tripe ionization as a dot-dot-dot-dash-dashed line; radiative decay as a solid line, and radiationless decay as a dotted line.

Chapter 3

Code structure and methodology

This chapter explains the Python code PlasmaFit developed for this thesis. The files and their relation are explained and the databases are presented. With these, it is detailed how the code processes them and presents the GUI's. All the possible inputs and functions are shown, then, a flowchart the process of determining the theoretical profile. Lastly, the implementation of the LM algorithm is explained.

3.1 Software description

A code capable of collecting databases and determining the CSD of x-ray spectra named PlasmaFit was developed. It is composed by seven .py modules and three folders (see Fig 3.1). The first folder "18", representing the atomic number for Ar, contains the database folder of the transition energies and cross section values for different processes. The second folder named "Experimental data" includes the .csv file of the measured x-ray spectrum from SIMPA. The transfer function folder keeps the intensity distribution .csv files to be loaded by the user.

In Python, .py modules can access defined functions from other modules by using the "import" statement. Fig. 3.2 shows how the seven modules are connected through imports. In blue are the .py modules and in white are the imported functions. The SpectraSimulation.py starts the code, with the PlasmaFit.py being the main operating module. It loads the database from Load.py and presents the main GUI. The user then chooses to calculate a simple plot from Calculation.py or use the LM algorithm with LMFit.py (and consequently CalculationLite.py - a simpler module of Calculation.py for extensive use). Both plotting modules require Functions.py with functions for the theoretical spectrum calculation. The packages used for the GUI's and plotting are TkInter and Matplotlib, respectively.

As SpectraSimulation.py is run, a periodic table is presented where the user selects

the element they wish to work with (see Fig. 3.3a). An option window appears with the different parameters the user can retrieve (Fig. 3.3b; only the "Plasma Diagnostics" button was developed in this work). Upon selecting the "Plasma Diagnostics" button, the code attempts to load the database inside a folder numbered by the atomic number chosen in the periodic table. The PlasmaFit.py's GUI (Fig. 3.5) where most the work is done will only be presented if the database is properly loaded, otherwise an error message box informing the user the issue with the database. Fig. 3.4 shows a flowchart with the organization of the code once the user opens it, up to loading the PlasmaFit.py's GUI.

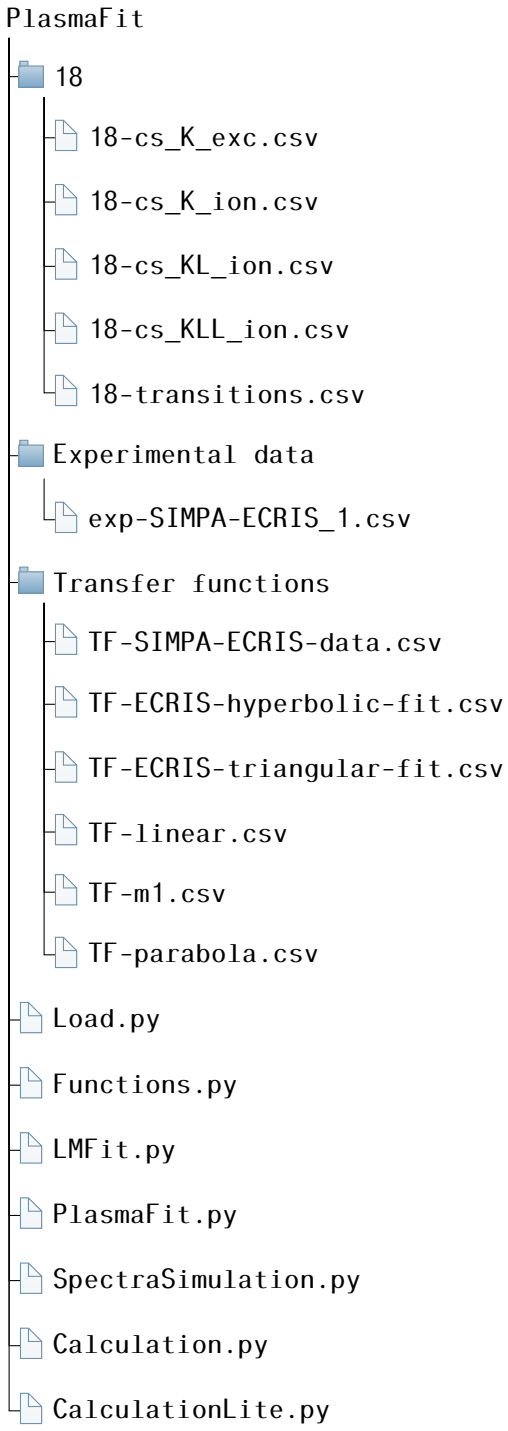

Figure 3.1: Tree of the "PlasmaFit" folder showing the relevant files to this work. The main folder has the program SpectraSimulation.py alongside other modules responsible for different aspects of the code.

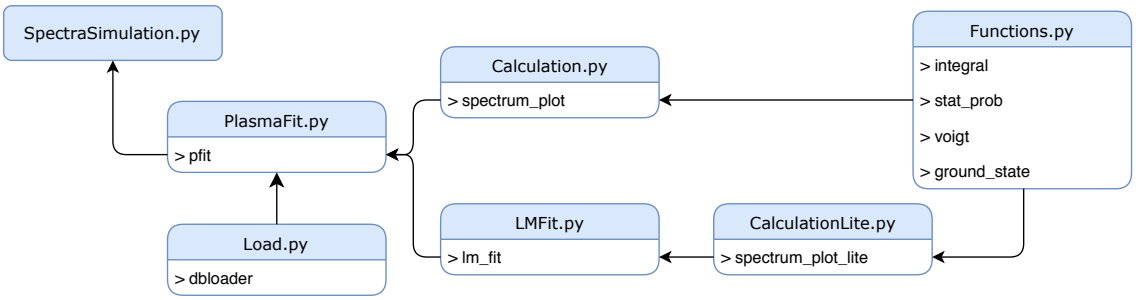

Figure 3.2: Scheme of the imports between the modules.

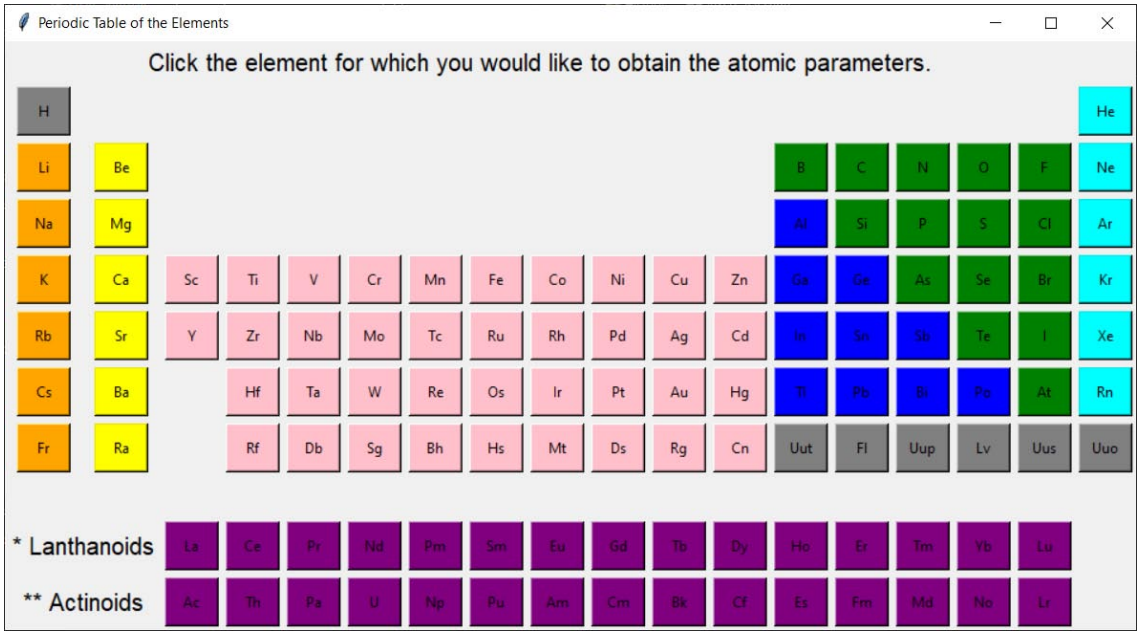

(a) Periodic table with the elements to choose from.

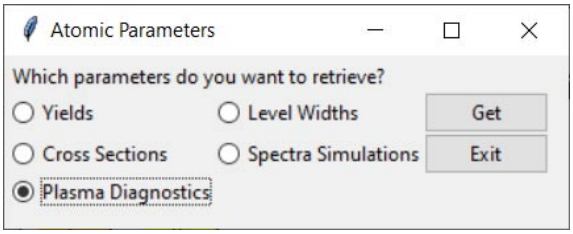

(b) Window with the different parameters to retrieve.

Figure 3.3: GUI's after starting SpectraSimulation.py. The first window (a) is a periodic table requesting the element to work with. Subsequently, the second window (b) loads asking which parameters to obtain. Only "Plasma Diagnostics" belongs to this work.

3.2 Database

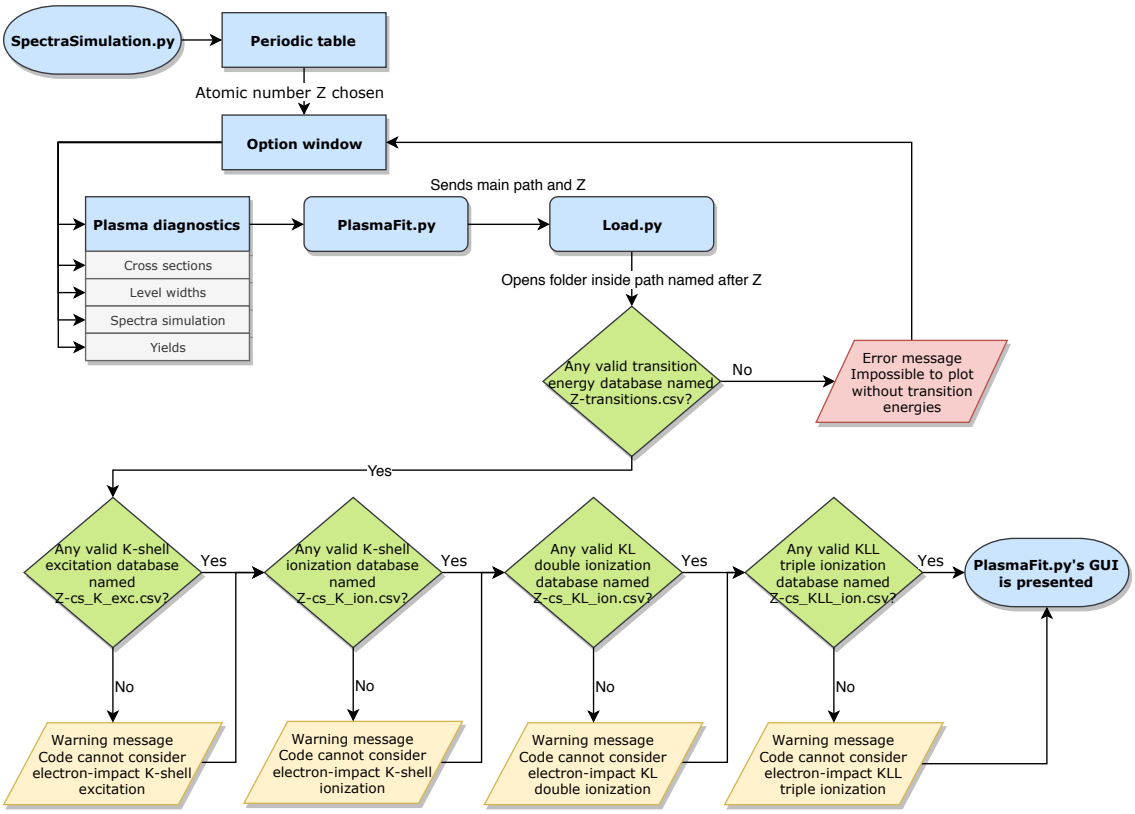

Figure 3.4: Flowchart of events from the loading of SpectraSimulation.py up to the display of the main GUI in PlasmaFit.py. The code starts by requesting an element to work with. Then, with an option window, the user can select different parameters to retrieve. Only "Plasma diagnostics" was done in this work. Load.py searches the databases for the element chosen. If no transition energy database is valid, the code will go back to the option window.

For the code to work, the database folder main requirement is to have at least the "Z-transitions.csv" file, with "Z" being the corresponding atomic number. This file alone allows for at least the stick plots of the transition energies. It contains a set of transitions which include the charge-state, the initial and final levels, the transition energies, the transition rate and its yield. Tab. 3.1 shows the transitions used in this work. The transition yield is calculated as the probability that a given transition occurs, taking into account not only the radiative transition rate but also the possibility that the initial level decays through a radiationless transition. The radiative and radiationless transition energy, transition probability, fluorescence yield values, and radiationless transition probabilities were calculated with the MCDFGME code and taken from [81].

The other .csv files correspond to the cross section values for different transition energies responsible for the excited states in the initial transition database. The files should be named "Z-cs_K_exc.csv", "Z-cs_K_ion.csv", "Z-cs_KL_ion.csv" and "Z-cs_KLL_ion.csv". Respectively, they represent the database for the K-shell excitation and ionization, KL

and KLL ionization. After the code checks if the files exist and loads them successfully, only then the user is able to calculate with the processes available. Tab. 3.2 and 3.3 show the partial tables for the excitation and ionization data kept in the files. The cross section values for electron-impact phenomena were determined according to Sec. 2.4, with the ionization energies also obtained from the MCDFGME code.

The cross section values are calculated according to the parameters from the Gauss-Laguerre integration (Eq. 2.12; Ref. [78]) in the form

$$\int_0^\infty e^{-x} f(x) dx \approx \sum_{i=1}^{n} w_i f(x_i) \tag{3.1}$$

Where x_i is the i^{th} root of the Laguerre polynomial $L_n(x)$, and the weight w_i is given by

$$w_i = \frac{x_i}{(n+1)^2 [L_{n+1}(x_i)]^2} \tag{3.2}$$

Since in this work we consider both non-Maxwellian and Maxwellian distributions within the plasma, two sets of 20 cross sectional values are kept for each transition at cold and hot temperatures ($kT = 1$ keV and $kT = 20$ keV respectively) for each root of the Laguerre polynomial and its weight. For a non-Maxwellian plasma, it is possible to use a linear combination of Maxwellian distributions for different temperatures. Another option would be resorting to different energy distributions, like κ-distributions detailed in [82].

Table 3.1: Table of the 28 transition energies (TE), transition rates (TR) and radiative transition yields in the database. The charge-states (CS), the initial and final states with the electronic configuration and LSJ terms are also stored. The number of transitions retrieved from the database depends on the energy region of the spectra that we want to simulate.

CS	Initial config.		Final config.		TE (eV)	TR (s^{-1})	Yield
16+	1s2p	$^3P_1$	$1s^2$	$^1S_0$	3123.37	1.81×10^{12}	1.00×10^{0}
	1s2s	$^3S_1$		$^1S_0$	3104.17	4.78×10^{6}	1.00×10^{0}
15+	1s2s2p	$^2P^1_{1/2}$	$1s^22s$	$^2S_{1/2}$	3112.40	8.65×10^{13}	7.32×10^{-1}
		$^2P^2_{1/2}$		$^2S_{1/2}$	3125.37	1.97×10^{13}	1.65×10^{-1}
		$^2P^1_{3/2}$		$^2S_{1/2}$	3114.15	1.00×10^{14}	9.12×10^{-1}
		$^2P^2_{3/2}$		$^2S_{1/2}$	3125.90	6.77×10^{12}	5.62×10^{-2}
		$^4P_{1/2}$		$^2S_{1/2}$	3086.69	1.64×10^{11}	9.47×10^{-1}
		$^4P_{3/2}$		$^2S_{1/2}$	3087.55	4.50×10^{11}	9.83×10^{-1}
14+	$1s2s^22p$	$^1P_1$	$1s^22s^2$	$^1S_0$	3091.79	9.81×10^{13}	4.28×10^{-1}
	$1s2s2p^2$	$^1S_0$	$1s^22s2p$	$^1P_1$	3090.93	5.29×10^{13}	1.79×10^{-1}
		$^1S_0$		$^3P_1$	3119.25	4.07×10^{9}	1.38×10^{-5}
		$^1P_1$		$^1P_1$	3088.82	1.51×10^{14}	7.19×10^{-1}
		$^1P_1$		$^3P_2$	3115.31	7.51×10^{9}	3.58×10^{-5}
		$^1P_1$		$^3P_1$	3117.15	7.90×10^{9}	3.76×10^{-5}
		$^1P_1$		$^3P_0$	3118.48	5.37×10^{10}	2.56×10^{-4}
		$^1D_2$		$^3P_2$	3102.36	3.10×10^{12}	1.42×10^{-2}
		$^1D_2$		$^3P_1$	3104.19	1.13×10^{11}	5.20×10^{-4}
		$^3S_1$		$^3P_2$	3097.40	3.15×10^{13}	2.99×10^{-1}
		$^3S_1$		$^3P_1$	3099.24	1.41×10^{13}	1.35×10^{-1}
		$^3S_1$		$^3P_0$	3100.57	3.73×10^{12}	3.55×10^{-2}
		$^3P^2_0$		$^3P_1$	3103.80	9.38×10^{12}	5.01×10^{-2}
		$^3P^1_1$		$^3P_0$	3085.80	7.82×10^{13}	3.89×10^{-1}
		$^3P^2_1$		$^3P_2$	3103.54	1.13×10^{13}	8.92×10^{-2}
		$^3P^2_1$		$^3P_1$	3105.37	1.65×10^{11}	1.30×10^{-3}
		$^3P^2_1$		$^3P_0$	3106.70	7.14×10^{11}	5.62×10^{-3}
		$^3P^1_2$		$^3P_1$	3087.37	4.59×10^{12}	2.08×10^{-2}
		$^3D_1$		$^3P_1$	3086.07	5.39×10^{13}	3.14×10^{-1}
		$^3D_1$		$^3P_0$	3087.40	1.38×10^{11}	8.02×10^{-4}

Table 3.2: Table showing the excitation energies for different initial and final configurations in the database. In italic blue, a metastable configuration was introduced manually, as the original database only had initial levels that are reachable through excitation and single, double and triple ionization, from the ion ground state.

CS	Initial config.		Final config.		Excitation energy (eV)
16+	$1s^2$	$^1S_0$	1s2s	$^3S_1$	3104.1605
		$^1S_0$	1s2p	$^3P_1$	3123.37
15+	$1s^22s$	$^2S_{1/2}$	$1s2s^2$	$^2S_{3/2}$	2733.41041
		$^2S_{1/2}$	1s2s2p	$^4P_{1/2}$	3086.69
		$^2S_{1/2}$	1s2s2p	$^4P_{3/2}$	3087.55
		$^2S_{1/2}$	1s2s2p	$^2P^1_{1/2}$	3112.40
		$^2S_{1/2}$	1s2s2p	$^2P^1_{3/2}$	3114.15
		$^2S_{1/2}$	1s2s2p	$^2P^2_{1/2}$	3125.37
		$^2S_{1/2}$	1s2s2p	$^2P^2_{3/2}$	3125.90
14+	$1s^22s^2$	$^1S_0$	$1s2s^22p$	$^1P_1$	3091.95
	$1s^22s2p$	*$^1P_1$*	*$1s2s2p^2$*	*$^1S_0$*	*3092.90*

Table 3.3: Table showing the ionization energies for different electron-impact ionizations and different initial and final configurations in the database. In italic blue, a metastable configuration was introduced.

Ionization	Initial config.	Final config.	Ionization energy (eV)
K	$1s^22s^22p$	$1s2s^22p$	3842.3588
	$1s^22s^2$	$1s2s^2$	3941.7821
	$1s^22s$	1s2s	4030.5030
	$1s^22s2p^2$	*$1s2s2p^2$*	*3829.5197*
KL	$1s^22s^22p^2$	$1s2s^22p$	4518.32962
	$1s^22s^22p^2$	$1s2s2p^2$	4518.32962
	$1s^22s^22p$	1s2s2p	4693.04915
	$1s^22s^22p$	$1s2s^2$	4693.12013
	$1s^22s^2$	1s2s	4872.04086
KLL	$1s^22s^22p^3$	$1s2s^22p$	5137.08393
	$1s^22s^22p^3$	$1s2s2p^2$	5137.08393
	$1s^22s^22p^3$	$1s2p^3$	5189.73351
	$1s^22s^22p^2$	1s2s2p	5379.30797
	$1s^22s^22p^2$	$1s2s^2$	5379.37895
	$1s^22s^22p^2$	$1s2p^2$	5414.20069
	$1s^22s^22p$	1s2s	5628.06260
	$1s^22s^22p$	1s2p	5647.04959

3.3 PlasmaFit.py

The main GUI is presented with the module PlasmaFit.py, shown in Fig 3.5.

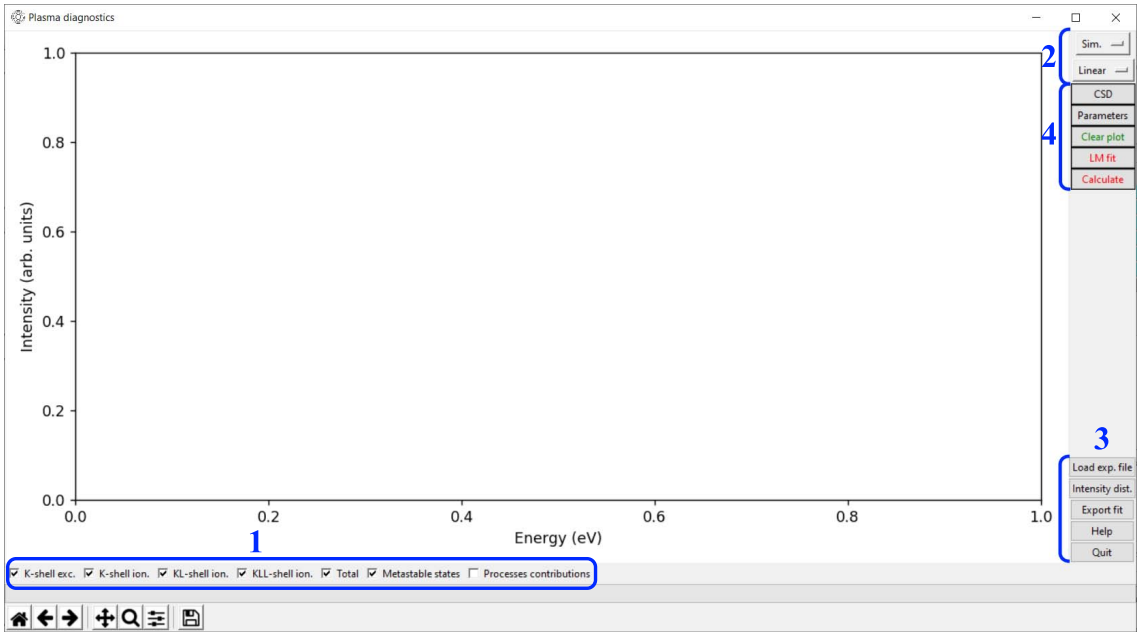

Figure 3.5: Main GUI from PlasmaFit.py, highlighting four sections with the possible inputs from the user.

3.3.1 Inputs

Once Load.py successfully loads the cross section databases, section 1 from Fig. 3.5 automatically checks the processes that are available in the database. If, for a certain process, there is a file missing or it does not correspond to the format chosen, the box will provide a warning message informing the user that it is impossible to consider the process. The "Metastable states" box starts checked meaning it considers non-ground initial states as long as these are stored in the database as metastable states. The "Processes contributions" button starts unchecked and shows lines for each single process considered (Fig. 4.4).

Section 2 shows two option buttons. The topmost option entails the type of spectrum to display, whether it is a stick plot or a simulated one as a pseudo-Voigt profile. The section's bottom option menu represents the y-axis scale, between linear and logarithmic.

Section 3 contains five buttons. From top to bottom, the first button allows the user to select an experimental data file in the .csv format. This file must contain the energy and intensity values in the first and second columns, with the respective but optional uncertainty values placed in the third and fourth columns. The transfer function is loaded in the second button, with it also necessarily being in the .csv format. The first two columns in this file must refer to the energy and intensity values which will then be normalized. After loading, it is displayed in a subplot in the top-left corner. In case a theoretical spectrum is displayed, any changes to the transfer function are automatically

applied. The "Export fit" and "Help" buttons are still in the making, with the "Help" button displaying an information message box referencing to this thesis work, which later could be improved to a user's guide. The "Quit" button closes the window.

Lastly, section 4 contains another five buttons. The green "Clear plot" button resets and clears the plotting area. The "CSD" button displays another GUI shown in Fig. 3.6. By default, a set of suggested ions and CSD is presented. A global dictionary "csd" stores the ions and its CSD. Updating is done by either pressing the enter key or the "Save" button.

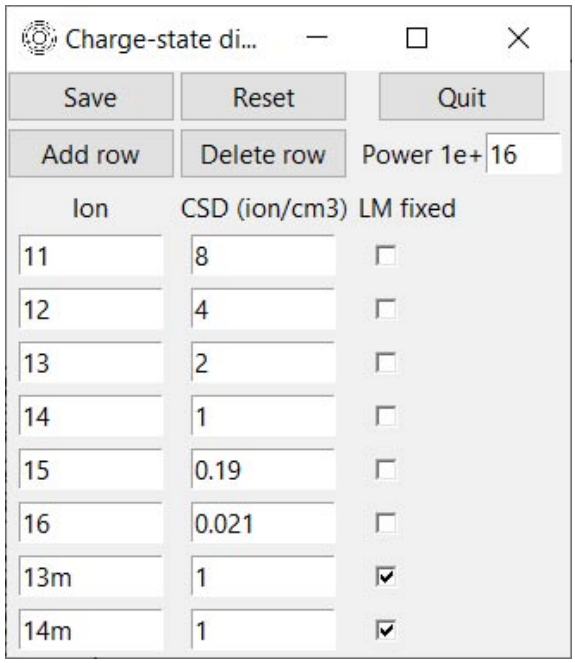

Figure 3.6: CSD GUI from PlasmaFit.py, showing the CSD the user can input. The "Add row" and "Delete row" buttons allow the user to insert or remove an ion. Any box checked in the "LM fixed" column fixes the parameter during the LM calculation.

The "Parameters" button opens a window shown in Fig. 3.7. This GUI allows the user to change parameters for the pseudo-Voigt profile such as the Gaussian and Lorentzian widths as well as the fraction between them. It is also possible to change the x-axis plotting step, as well as the energy shift for a better correspondence with experimental data. The minimum and maximum energy determine the range in which the transition database is queried. The fraction between the Maxwellian and non-Maxwellian distribution can be altered as well. When it comes to the background noise, three different methodologies are possible. The first two options implement a fixed horizontal offset across the plotting range, where the "Fixed" radio button lets the user choose the background noise value, and the "Min. χ^2" tries to find the best fit background noise, by attempting different offsets until the χ^2 value is minimized. Lastly, the third radio button allows for a background with a slope. If either a theoretical spectrum or experimental data is displayed, the user can simply click in two different points in the plotting area and an offset will be

determined. With no plot, a window will be displayed requesting the m and b parameters of the $y = mx + b$ equation. The normalization row allows the theoretical spectrum to be fixed to a certain point. With experimental data present, the "Data point" button allows the user to select an energy point in which the calculated plot will be the same as the experimental data. The "Coordinate" button lets the user either click on a coordinate to normalize or input the coordinates in a separate window, depending on if anything is being displayed in the plotting area. These parameters can be saved by either clicking on the "Save" button or pressing the enter key. This GUI is firstly presented with suggested default inputs.

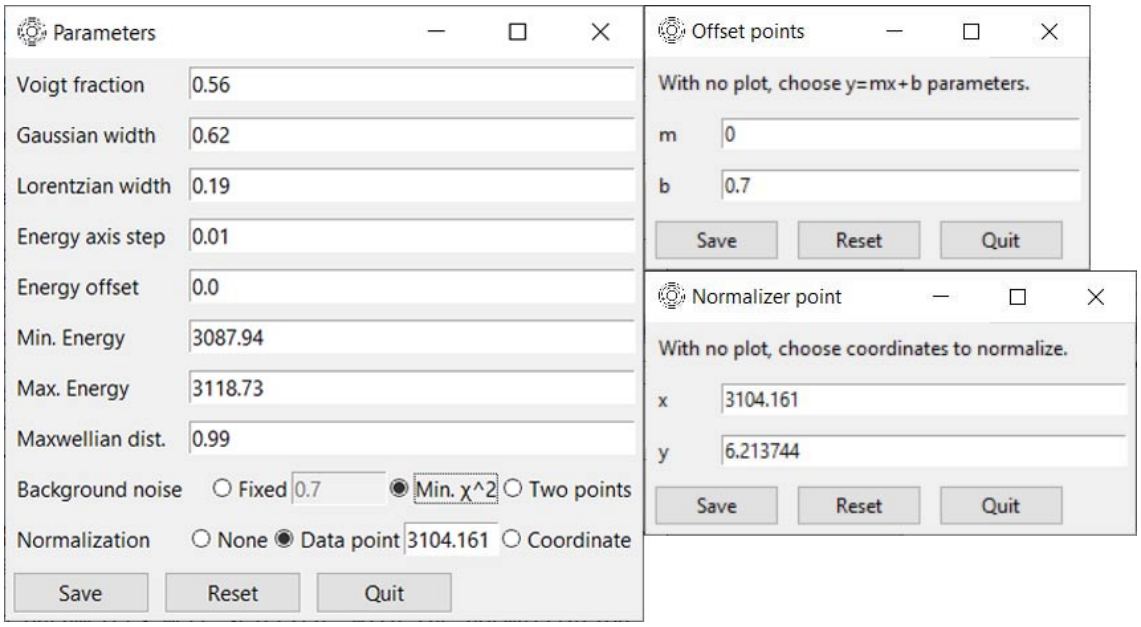

Figure 3.7: Parameters GUI's from PlasmaFit.py, showing the parameters the user can input. The two windows on the right side are shown in case no plotting is done, allowing the user to manually insert the parameters for the background noise and normalization. With a plot shown, the user can simply click on the coordinates instead.

The red "Calculate" button sends all the inputs to the function spectrum_plot() in Calculation.py, and plots the theoretical spectrum accordingly. If the buttons "CSD" or "Parameters" were not changed, a warning message box will inform the user that default parameters and CSD values set by the developer will be used. Another warning message will show if no instrumental transfer function was loaded. The red "LM fit" button only works if there is experimental data for a theoretical spectrum to fit. It starts the LM algorithm in LMFit.py and returns a CSD from the best fit the algorithm could reach. Once the user opens the CSD window again, it will now be filled with the new improved CSD.

In any case, if a theoretical spectrum is shown, any alteration in sections 1 or 2 or in the buttons "CSD" and "Parameters", will immediately be adjusted accordingly. Any kind of impossible parameters are prevented to be saved such as negative energies, widths,

CSD, out of range Voigt or Maxwellian fractions and invalid characters by showing a warning message box justifying it.

3.4 Functions.py

The Functions.py module contains a series of functions which are used to determine the theoretical spectrum and create a pseudo-Voigt profile based on the line intensities. The following subsections provide a functioning overview.

3.4.1 Integral

A simple function resolving the integral from Eq. 2.12 is coded with the Gauss-Laguerre integration method alongside the physical constants necessary.

Listing 3.1: Definition of the function integral() in Functions.py where it calculates the integral in Eq. 2.12.

```
1  from numpy import asarray, exp, sqrt, sum
2
3  kt_c = 1e3 #kT for cold temp. (could set as inputs in a further version)
4  kt_h = 2e4 #kT for hot temp.
5  m_e = 9.1093835611e-31 #Electron mass
6  mec2 = 5.10998946131e5 #mc^2 for electron
7  e_j = 1.602176620898e-19 #Charge of an electron
8  c_Mw = 2.67618617422916e16 #Maxwellian coeff.
9  c_nMw = 8.70366940390332e28 #Non-Maxwellian coeff.
10
11 x_i = asarray([0.0705399, 0.372127, 0.916582, 1.70731, 2.7492, 4.04893, 5.61517, 7.45902,
       ↪  9.59439, 12.0388, 14.8143, 17.9489, 21.4788, 25.4517, 29.9326, 35.0134, 40.8331,
       ↪ 47.62, 55.8108, 66.5244])
12 w_i = asarray([0.168747, 0.291254, 0.266686, 0.166002, 0.0748261, 0.0249644, 0.00620255,
       ↪ 0.00114496, 0.000155742, 1.54014e-05, 1.08649e-06, 5.33012e-08, 1.75798e-09,
       ↪ 3.7255e-11, 4.76753e-13, 3.37284e-15, 1.15501e-17, 1.53952e-20, 5.28644e-24,
       ↪ 1.65646e-28])
13
14 #Calculates the integral of Maxwellian and non-Maxwellian dist. of the plasma with hot
       ↪ and cold temp.
15 def integral(hw_min, cross_section_c, cross_section_h, fraction):
16   E_i = x_i*kt_c + hw_min
17   f_Mw = sum(w_i*E_i*sqrt(e_j)*(sqrt(E_i+2*mec2)/(E_i+mec2))*cross_section_c)*c_Mw*exp(-
         ↪ hw_min/kt_c)
18
19   E_i = x_i*kt_h + hw_min
20   f_nMw = sum(w_i*(E_i*e_j)**1.5*(1+E_i/(2*mec2))**1.5*cross_section_h)*sqrt(2/m_e)*c_nMw
         ↪ *kt_h*e_j*exp(-hw_min/kt_h)
21
22   n_rate = fraction*f_Mw + (1-fraction)*f_nMw
23   return n_rate
```

3.4.2 Statistical weight

As an ion in an ECRIS plasma suffers electron-impact ionization, the change in the electronic configuration contains different possible final LSJ terms. Each of these terms have $2j+1$ possible states due to the different magnetic quantum numbers. Therefore, when one calculates the number of radiative emissions from a specific LSJ term, through ionization processes, it must be accountable that the initial levels will not always decay via the emission of a photon. The probability for this is explained in Eq. 2.24. The percentage is then multiplied by the event rate of a certain process in order to get the accurate population of ions in the specific excited state in the database (Eq. 2.12).

To code this, a simple way to calculate the sum of $2j+1$ states was used. Each orbital s, p, d, and f was attributed to a row in Pascal's triangle based on the number of orbital types. One for s, as it is spherically shaped, three for p (namely p_x, p_y, p_z), five for d and seven for f. The number of orbitals n is associated with the row $2n$ in Pascal's triangle and the number of electrons is related to entry k. The code then calculates the binomial coefficients as

$$\binom{2n}{k} = \frac{(2n)!}{k!(2n-k)!} \tag{3.3}$$

The function stat_prob() was made in Functions.py for this purpose. By receiving an LSJ term and electronic configuration, the code proceeds to multiply the number of arrangements in each orbital and returns the probability of a certain process to result in the LSJ term.

Listing 3.2: Definition of the function stat_prob() in Functions.py where it calculates the probability of an electronic configuration to be in a certain LSJ term. The terms are read in the format of '[LSJ]'.

```
from math import factorial

def nCk(n,k):
  f = factorial
  return f(n) // f(k) // f(n-k)

def orb(orbital): #Input string with orbital and nr of electrons (e.g. p6)
  order = ['s', 'p', 'd', 'f']
  l = orbital[0] #Assigns orbital to l
  n = (4*order.index(l) + 2) #Number of electrons that fit in the orbital (2n+1)*2 (spin
      ↪ up/down)
  k = int(orbital[1]) #Assigns nr of electrons in the orbital
  r = nCk(n, k) #Combination of electronic arrangements possible in that orbital
  return r

def stat_prob(lsj_i, state):
  if len(lsj_i) == 5: #Ask if it is in [LSJ] with 5 spaces (no fractions in J)
    j_i = 2*int(lsj_i[-2]) + 1
  else: #Else there are fractions ([1P1/2] for example)
    fraq = int(lsj_i[3]) / int(lsj_i[5])
```

```
20      j_i = 2*frac + 1
21
22    n = int((len(state)-1)/4) #Know how many orbitals there are based on the length of the
          ↪ string
23    orbital = []
24    for i in range(n + 1):
25      orbital.append(state[1 + 4*i] + state[2 + 4*i]) #Append orbital and nr of electrons
            ↪ in it
26    sum_j = 1
27    for i in range(len(orbital)):
28      sum_j *= orb(orbital[i]) #Multiply by the binomial coeff for every orbital & nr of
            ↪ electrons
29    return j_i/sum_j
```

3.4.3 Ground states checker

As stated in Sec. 2.4.5, the initial states in the transition energies, must come from processes in the ground state, unless the plasma that originated the spectrum is hot enough to have highly populated excited states. A boolean function named ground_state() in Functions.py was implemented to verify if it is possible to originate an excited state through any given process from its fundamental state (see List. 3.3). It is used while the plotting code runs every relevant transition energy in the database, and tries to calculate from the cross section databases of the processes.

The function works backwards, from the excited state it attempts different possibilities to reach a ground state through the inverse of the requested process (K-shell excitation and single to triple ionization in the K and L shells). The first orbital must be "1s", because every considered process involves adding just one electron to the K-shell orbital. For example, we cannot have the state starting with "$2s^*$..." because "$1s2s^*$" can never be a ground state, or even "$1s^2$..." as it will result in the impossible "$1s^3$" configuration. In the future, for a more general process, we can allow K-shell double and triple excitation or ionization, meaning that the two 1s electrons can, in principle, be removed during the collision process. If the function returns false, the code will not attempt to look for cross section values for that process in the transition queried. *A posteriori*, metastable states were introduced into the database. If the user chooses to consider metastable states, once the ground_state() function expectedly returns false, it will query the cross section values for any metastable states in the specific transition.

Listing 3.3: Definition of the function ground_state() in Functions.py where it checks if an excited state can come from a ground state through a process n (n = 0, 1, 2, 3 correspond to K-shell excitation and K, KL, KLL ionization respectively). The triple ionization query was not shown as it is a longer version of double-KL ionization with the same logic.

```
ground_states_list = ['1s1','1s2','1s2␣2s1','1s2␣2s2','1s2␣2s2␣2p1', '1s2␣2s2␣2p2','1s2␣2
    ↪ s2␣2p3','1s2␣2s2␣2p4','1s2␣2s2␣2p5','1s2␣2s2␣2p6']
def ground_state(state_exc, n): #Check if ground state phase is possible with n
    ↪ ionizations (0 is excitation)
  s = list(state_exc)
  if int(s[0]) == 2 or s[1] != 's' or int(s[2]) => 2: return False #We can't have an
      ↪ orbital start with 2s or 2p, so s[0] and s[1] must be 1 and s, and we can't have
      ↪  1s3 as these are all impossible to be a ground state
  s[2] = str(int(s[2])+1) #Adds an electron to the 1s orbital

  if n == 0: #Through excitation K
    s[-1] = str(int(s[-1])-1) #Removes an electron in the last position
    if s[-1] == '0': #If there is no electrons, it removes the orbital
    s = s[:-4]
    s = ''.join(s)
    return s in ground_states_list #It does not try to remove electron in the middle,
        ↪ because that immediately makes it impossible to be ground state

  if n == 1: #Through ionization K
    s = ''.join(s)
    return s in ground_states_list #Was already added to K-shell

  if n == 2: #Through double ionization KL
    s[6] = str(int(s[6])+1) #Considers adding in the orbital next to the first one
    s = ''.join(s)
    if s in ground_states_list: return True
    elif len(s) == 11: #If there is a third orbital it adds one there instead
      s = list(s)
      s[6] = str(int(s[6])-1)
      s[10] = str(int(s[10])+1) #If there is more, it adds one in the last position
      s = ''.join(s)
      return s in ground_states_list
    else: #There is not a third orbital, then one is added
      s = list(s)
      s[6] = str(int(s[6])-1) #Remove it to transfer for new orbital
      s.append('␣')
      s.append('2')
      s.append('p')
      s.append('1') #Adds orbital 2p with one electron
      s = ''.join(s)
      return s in ground_states_list #Last attempt
  (...)
  return False #This is coded as a precaution in case nothing is ever returned above
```

3.4.4 Voigt profile

A Voigt profile is a distribution useful for x-ray spectroscopy since it is flexible enough for a variety of peaks that may show in an experimental spectrum. It is a convolution of the Gaussian and Lorentzian distributions, the former relating to Doppler broadening and instrumental resolution and the latter to lifetime broadening. Each transition energy presented in a given spectrum will basically correspond to the centroid of a Voigt distribution, with the width given by the combination of the inverse of the initial state lifetime and the experimental broadening and amplitude by the line intensity. Afterwards, all functions are summed up.

Due to the high computational demand in an actual Voigt profile, an approximation will be used with a linear combination of both Gaussian and Lorentzian distributions. This is called a pseudo-Voigt profile and is defined by

$$\boldsymbol{V(A,x,u,\gamma_G,\gamma_L,\alpha)} = A \times [\alpha \times \boldsymbol{G(x,u,\gamma_G)} + (1-\alpha) \times \boldsymbol{L(x,u,\gamma_L)}] \tag{3.4}$$

Where A is the amplitude (line intensity), x a coordinate in the horizontal axis, u the center value (transition energy), γ_G the Full Width Half Maximum (FWHM) for the Gaussian function and γ_L the FWHM for the Lorentzian function. With the relation between the standard variation σ_G and the FWHM γ_G

$$\sigma_G = \frac{\gamma_G}{2\sqrt{2\ln 2}} \tag{3.5}$$

The normalized Gaussian distribution is given as

$$\boldsymbol{G(x,u,\gamma_G)} = \frac{1}{\sigma_G\sqrt{2\pi}} \exp\left[-\frac{(x-u)^2}{2\sigma_G^2}\right] \tag{3.6}$$

And the normalized Lorentzian distribution

$$\boldsymbol{L(x,u,\gamma_L)} = \frac{\gamma_L}{2\pi\left[(x-u)^2 + \left(\frac{\gamma_L}{2}\right)^2\right]} \tag{3.7}$$

In Fig. 3.8, both distributions and the pseudo-Voigt profile are presented. For $\alpha = 1$ the Voigt function is equal to the Gaussian distribution and for $\alpha = 0$, it is a fully Lorentzian one. Inside Functions.py, the function voigt() is used to calculate the pseudo-Voigt profile as seen in List. 3.4.

Listing 3.4: Definition of the pseudo-Voigt function in Functions.py which is used for every transition energy intensity calculated.

```
from numpy import exp, pi, sqrt

def voigt(A, x, u, width_gauss, width_lorentz, fraction):
  sigma_gauss = width_gauss/(2*sqrt(2*log(2)))
  gauss = exp(-.5*((x-u)/sigma_gauss)**2)/(sigma_gauss*sqrt(2*pi))

  lorentz = width_lorentz/(2*pi*((x-u)**2+(width_lorentz/2)**2))

  return A*(fraction*gauss+(1-fraction)*lorentz)
```

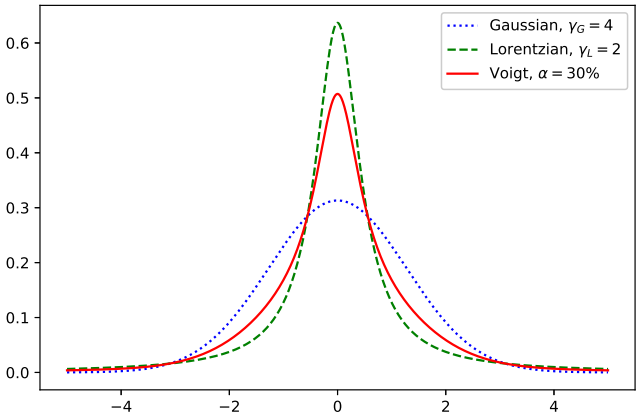

Figure 3.8: Graphic of a pseudo-Voigt profile showing both distributions. The green dashed line shows a Lorentzian distribution ($\alpha = 0$) with width 2 and the blue dotted line a Gaussian one ($\alpha = 1$) with width 4. The red line represents the pseudo-Voigt profile - the linear combination of both functions as 30% Gaussian and 60% Lorentzian.

3.5 Theoretical spectrum calculation

Upon clicking the "Calculate" button, the code will check if a transfer function was loaded and the CSD and other parameters were saved. Otherwise standard values chosen by the developer are used. Next, all the inputs are sent to a function in Calculation.py called spectrum_plot(). The flowchart in Fig. 3.9 shows the code sequence logic.

The function starts by clearing the spectrum plot and reloading the experimental data (if any). A domain is set between the minimum and maximum energy values from the "Parameters" GUI as well as the background noise offset. The transition database is reduced between the energies comprehended in the domain. The line intensities are then calculated.

3.5.1 Line intensities

The intensities are calculated for each transition energy of interest and through the electron-impact processes chosen by the user. First, the ground_state() function returns true if a given process can originate an excited state from a ground state. If so, a query within the cross section database for a match between the excited states starts. A match will result in the calculation of the integral from Eq. 2.12 followed by the line intensity of Eq. 2.26. In the case of ionization, the latter equation is also multiplied by the statistical weight (Sec. 3.4.2).

In the cross section database, the last index has included a specific transition energy, indicating that it is a metastable state (all others have 0). If the ground_state() returns false for a process and the user wants to include metastable states, the code will then seek for the last index and see if it matches with the transition energy in question. If so, the calculation proceeds as explained before.

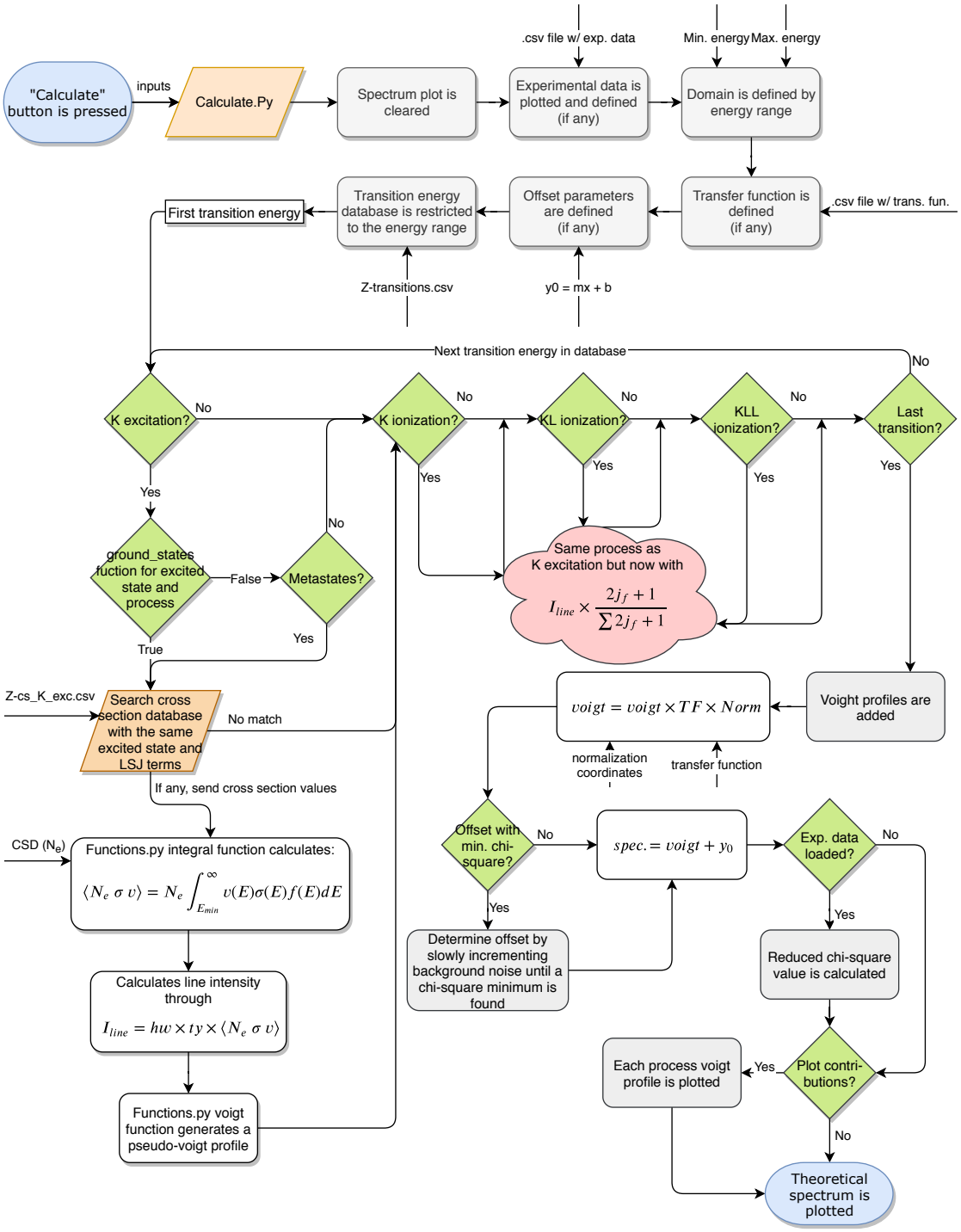

Figure 3.9: Flowchart of events after clicking the "Calculate" button in PlasmaFit.py's GUI. All inputs are sent to Calculate.py and a rundown of the transition database calculates the line intensities based on the cross section database of the considered processes. The code can be read in List. 3.5.

Listing 3.5: Calculation of line intensities and creation of a pseudo-Voigt profile. Only electron-impact K-shell ionization is shown, however, the same logic is applied for the other processes.

```
from SFunctions import ground_state, integral, stat_prob, voigt
from numpy import arange, zeros

x = arange(hw_min, hw_max, step) #Domain arranged
voigt_K_ion_profile = zeros(len(x))
counts_K_ion = []
hw_K_ion = []
for i in range(len(hw_trans)): #Scans the transition energy database
  (...) #K-shell excitation
  if kion: #If process K-shell ionization is chosen by user
    if ground_state(hw_trans[i,5],1): #State, if process can come from ground state
      for j in range(len(cs_K_ion)): #Scan through the cross section database
        if hw_trans[i,5] == cs_K_ion[j,2]: #If the states match then calculate
          n_rate = integral(cs_K_ion[j,0], cs_K_ion[j,4], cs_K_ion[j,5], fraction_mw) #
              ↪ Calls for integral in Functions.py
          hw = hw_trans[i,0] #Transition energy
          ty = hw_trans[i,4] #Transition yield
          try: nq = csd.get(str(cs_K_ion[j,3] - 1)) * 10**csd.get('power') #Looks for the
              ↪ ion in the csd dictionary
          except: nq = 0 #Else return 0
          sp = stat_prob(hw_trans[i,7], hw_trans[i,5]) #Calculates 2J+1/sum(2J+1)
          counts_K_ion.append(n_rate * hw * ty * nq * sp) #Appends intensity
          hw_K_ion.append(i) #Appends index in the transition database

    elif metastates: #Else wonder if there's a metastate (only if user wants)
      for j in range(len(cs_K_ion)): #Same logic as before is applied
        if (cs_K_ion[j,-1] == hw_trans[i,0] and hw_trans[i,5] == cs_K_ion[j,2]): #Last
            ↪ index in database indicates if the cross section values is a metastate
          n_rate = integral(cs_K_ion[j,0], cs_K_ion[j,4], cs_K_ion[j,5], fraction_mw)
          hw = hw_trans[i,0]
          ty = hw_trans[i,4]
          try: nq = (csd.get(str(cs_K_ion[j,3] - 1)+'m') * 10**csd.get('power'))
          except: nq = 0
          sp = stat_prob(hw_trans[i,7], hw_trans[i,5])
          counts_K_ion.append(n_rate * hw * ty * nq * sp)
          hw_K_ion.append(i)
  (...) #KL and KLL ionizations
  if stick_sim = 'Sim.': #If user wants a pseudo-Voigt profile
    (...) #K-shell excitation
    if kion:
      for i in range(len(hw_K_ion)): #Profile making for K shell ionization
        voigt_K_ion_profile += voigt(counts_K_ion[i], x, hw_trans[hw_K_ion[i], 0] + hw0,
            ↪ width_gauss, width_loren, fraction_voigt)
    (...) #KL and KLL ionizations
    voigt_profile = (voigt_K_exc_profile + voigt_K_ion_profile + voigt_KL_ion_profile +
        ↪ voigt_KLL_ion_profile) #Sum of all the profiles
```

3.5.2 Transfer function

As discussed in Sec. 2.3.1, the ray-tracing Monte Carlo simulation histogram results shown in Fig 2.10 from Amaro [48] represents the experimental transfer function from the DCS used for the spectrum in this work. Since the vertical divergence of the maximum number of rays reaching the detector is not exactly zero (Fig. 2.11), a hyperbolic fit is deemed appropriate. However, as the code must be ready for different kinds of instrumental transfer functions, a simple cubic interpolation was implemented into the code once a transfer file is loaded. Nonetheless, both fits are saved in .csv format and can be loaded by the user (the program will do an interpolation over a hyperbolic fit, for example). Different transfer functions were saved in the folder to exemplify its usage and effect (linear equations, parabolas, etc...). List. 3.6 shows how a transfer function is defined and implemented in the final pseudo-Voigt profile.

Listing 3.6: Defining of the transfer function in Calculation.py after a file has been chosen and loaded by the user in PlasmaFit.py.

```
from numpy import arrange, genfromtxt, ones
from scipy.interpolate import interp1d #For the transfer function fit
(...)
if trans_file != '': #If a TF was loaded in PlasmaFit.py then trans_file will have a path
  def tf(x): #x is an array of the domain being worked with and returns y array
    data_tf = genfromtxt(trans_file, delimiter = ',')
    xtf = data_tf[:,0]
    ytf = data_tf[:,1]
    inter = interp1d(xtf, ytf/max(ytf), kind = 'cubic') #Transfer function fit w/
        ↪ normalization
    return inter(x)
else: #Else, no change in the TF
  def tf(x):
    return ones(len(x))

x = arange(hw_min, hw_max, step) #Domain with user selected energy intervals and step
(...) #Calculation of the voigt_profile
voigt_profile *= tf(x) #Profile now follows the intensity distribution
```

3.5.3 Normalization

The parameters also allow for normalization. Recapping from Fig. 3.7, "Data point", will fix the theoretical spectrum on the experimental data intensity point for the inserted energy value. The "Coordinate" option will normalize the theoretical spectrum for a specific energy and intensity coordinate. List. 3.7 shows how the normalization was coded.

Listing 3.7: Normalization of the final pseudo-Voigt profile with an experimental data point (y-axis value unknown) or for a specific coordinate.

```
from numpy import argmin

if norm_method == 'Data' and exp_data: #Look for the x to force the theoretical line on
    ↪ the experimental line
  dif_exp = abs(hw_exp - norm_x)
  n_exp = argmin(dif_exp) #Closest point between exp data and requested norm_x point
  dif_prof = abs(x - norm_x) #Same is done but for the voigt profile
  n_prof = argmin(dif_prof) #n_prof now is the voigt profile point closest
  normalization = (counts_exp[n_exp]-y0[n_prof])/voigt_profile[n_prof] #Removes y0 (
      ↪ offset) from exp data
  voigt_profile *= normalization #Multiply itself by the normalization factor

elif norm_method == 'Coor': #It will force theoretical line on (x,y) position
  dif_prof = abs(x - norm_x)
  n_prof = argmin(dif_prof) #Closest point between domain and requested norm_x point
  voigt_profile *= norm_y/voigt_profile[n_prof] #norm_y is y point to normalize
```

3.5.4 χ^2

With experimental data to compare to. Once the theoretical spectrum is calculated, the reduced chi-square is calculated with

$$\chi^2_{red} = \frac{1}{N-1}\sum_{i}^{N}\frac{(I_{theo}-I_{exp})^2}{\sigma^2_{exp}} \tag{3.8}$$

Where N is the number of experimental data, I_{exp} and I_{theo} the experimental and theoretical intensity values respectively and σ_{exp} the intensity experimental error.

With the "Min. χ^2" parameter chosen from Fig. 3.7, the code will calculate several χ^2 values for small increments of background noise. For quicker computation time, once there is a shift in the χ^2 value indicating a minimum, the code will keep that offset and add to the final spectrum. Nonetheless, if the shape of the background noise is too irregular, this may result in some local minima.

Listing 3.8: Calculation of the reduced χ^2 value with the determination of the background noise for the "Min. χ^2" parameter.

```
from numpy import arange, argmin, array, average, int

y0 = array(y0_m * x + y0_b) #Offset as an array to simply add to profile
if exp_data: #If there is experimental data
  if y0_method == 'Chi': #If min. chi2
    chi2_max = int(2e8) #High value to compare
    y = arange(min(counts_exp), average(counts_exp), step)
    for j in range(len(y)): #Minimizes chi2 based on different offsets y0
      chi2 = int(0)
      spectrum_csd = voigt_profile + y[j]
      for i in range(len(hw_exp)):
        dif = abs(x - hw_exp[i])
        n = argmin(dif)
        chi2 += (spectrum_csd[n] - counts_exp[i])**2/(counts_exp_err[i]**2*(len(hw_exp)-1)
            ↪ )
      if chi2 < chi2_max:
        chi2_max = chi2
        y0 = y[j] #New offset value
      else: break #Makes computation quicker but can cause local minimi
    chi2 = chi2_max
    spectrum_csd = voigt_profile + y0 #Profile w/ noise, y0

  else: #If no minimization of offset is asked
    spectrum_csd = voigt_profile + y0 #Profile w/ noise y0 set by the user
    chi2 = int(0) #Chi2 value between exp data and theoretical proceeds
    for i in range(len(hw_exp)):
      dif = abs(x - hw_exp[i])
      n = argmin(dif)
      chi2 += (spectrum_csd[n] - counts_exp[i])**2/(counts_exp_err[i]**2*(len(hw_exp)-1))
          ↪ #If there's no exp error, it will just divide by 1

else: spectrum_csd = voigt_profile + y0 #No exp data, profile w/ noise
(...) #Plotting
```

3.6 Levenberg-Marquardt (LM) algorithm

For an accurate CSD, the χ^2 value must be minimized between the theoretical spectrum and the experimental data. Manually, this can be a rather complex fitting task as it concerns many variables. Hence, a non-linear least-squares fitting model was implemented in the LMFit.py module where it employs the LM algorithm against experimental data.

The LM fitting method combines two other minimization approaches, the gradient descent and the Gauss-Newton (GN) method. Based on an initial guess of the optimal parameters, these methods work on finding an optimal solution by executing a series of calculations for different parametric values.

The gradient descent method attempts to reduce the sum of the squared errors by directing the parameters to its deepest descent. The GN method considers the least squares function as quadratic and changes the parameters towards the quadratic minimum. Instead of having these two methods on their own, the LM algorithm applies one of the two depending on how close to an optimal value it is. For distant guesses, the gradient descent is employed but once the parameters start to approach the ideal value, the algorithm changes to the GN method. This distance is given by the non-negative damping factor λ [83].

For functions with one global minimum, any of these methods can easily converge to the optimal value. However, with local minima, it is easy to converge into one of them and miss the global minimum. The LM fitting method produces some "jumps" wherein it attempts to escape a possible local minimum, making it appropriate for far from optimal initial guesses, compared to gradient descent or GN alone. Even more, the methods reach ideal results slower than their combination through the LM algorithm [84]. Notwithstanding, as seen in Chap. 4, a good enough guess must still be given and the algorithm may still return local minima. Some problems with the LM algorithm consist on their slow convergence for many parameters, and sometimes, none at all for very flat functions (see Refs. [85–87]).

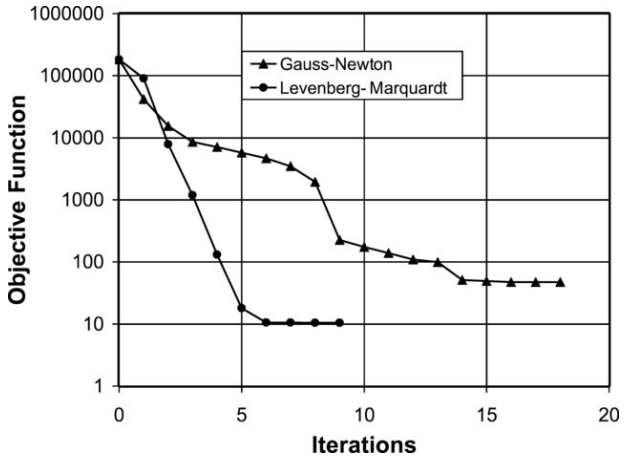

Figure 3.10: Convergence rate comparison between the LM and GN methods (circular shaped and triangular shaped symbols respectively) for a given minimization problem [88]. The LM algorithm converged to a better result with less iterations than the GN.

3.6.1 lmfit package

The lmfit package [89] provided the tools to execute the algorithm into the balance equation. Based on scipy.optimize.leastsq() and scipy.optimize, the package worked on adding useful improvements. The input CSD can be varied or fixed, with upper and lower bounds or even restricted to an expression. The minimize() function can easily apply different

fitting models by changing the "method" argument, increasing the confidence level of the obtained CSD.

Firstly, a function lm_res() takes in the parameters, the experimental data, and the domain where it calculates the theoretical spectrum and compares it against the experimental one. Some approaches return a simple residual subtraction ($model - measured$) or divide by some weighting factor ($(model - measured)/\epsilon$). An approach with the χ^2 is used with the weighting factor being the uncertainty in the data. The χ^2 is defined as

$$\chi^2 = \sum_i^N \frac{\left[I_i^{exp} - I_i^{theo}(CSD)\right]^2}{\epsilon_i^2} \tag{3.9}$$

Where I_i^{exp} is the experimental data intensity, $I_i^{theo}(CSD)$ the theoretical spectrum with CSD the ion CSD being optimized and ϵ_i the data uncertainty. In case the experimental data loaded does not include uncertainty values, ϵ_i will be considered $\sqrt{n_i}$ where n_i is the number of counts for energy i. The lm_res() is shown in List. 3.9.

Listing 3.9: LM residual function in LMFit.py which takes in the domain, experimental data and the CSD parameters. It then determines the theoretical spectrum with the changing parameters and returns the χ^2 value.

```
from CalculationLite import spectrum_plot_lite

ions = list(csd.keys())[1:] #list w/ the ion list in csd dictionary input by user
csds = list(csd.values())[1:] #list w/ the densities
fixeds = list(fixed.values()) #list whether or not the specific ion csd is to vary

def lm_res(params, x, data, counts_exp_err):
  for i in ions: #Cycles through all the input ions by the user
    csd[i] = params['nq' + i]
  #Quicker to compute than spectrum_plot from Calculate.py
  spectrum_csd = spectrum_plot_lite(*args) #Sends all inputs and the csd dictionary
  result = (data[1] - spectrum_csd)/counts_exp_err
  return result
```

The parameters and their optimization are shown in List. 3.10. The class "Parameters" is used to add the input CSD for the least-squares fit. The argument "vary" is assigned true or false depending on the "LM fixed" column from Fig. 3.6 being checked. Fixing the values will make the parameters unchangeable during the fit. Only a minimum value of 0 is enforced since restrictions have proven to be computationally demanding. Thus, having expressions defining the CSD (for instance a Gaussian distribution), albeit useful, are difficult to implement. The minimize() function calls the lm_res() function in List. 3.9 and sends the parameters as they are adjusted to fit the experimental data. Once the algorithm converges, the "csd" dictionary is updated to the new values, the spectrum is plotted, and the CSD is sent to the GUI of Fig. 3.6.

Listing 3.10: Code section from LMFit.py with the parameters initiation and other inputs for the application of the LM algorithm. The function minimize() calls the residual function shown in List. 3.9 and attempts to find the CSD which minimizes its return.

```
from numpy import arange, array, average, genfromtxt, sqrt
from lmfit import minimize, Parameters
from Calculation import spectrum_plot
from tkinter import messagebox

params = Parameters() #Parameters class assigned to params
for i in range(len(ions)): #Goes through every ion and assigns it to a parameter
  params.add('nq' + ions[i], value = csds[i], min = 0, vary = not fixeds[i]) #Restricted
      ↪ only to min=0. vary = False will fix parameter (checked box in LM fixed column)

x = arange(hw_min, hw_max, step) #Domain arranged
y0 = array(y0_m * hw_exp + y0_b) #Offset as an array to add to the profile
y = arange(min(data[1]), average(data[1]), step)

data_exp = genfromtxt(csv_file, delimiter = ',') #Loads experimental data
hw_exp = data_exp[:,0]
counts_exp = data_exp[:,1]
try: counts_exp_err = data_exp[:,3] #Attempts to assign uncertainty
except: counts_exp_err = sqrt(counts_exp) #If none, just do srt(n_i)
data = [hw_exp, counts_exp] #This is done in case data_exp contains uncertainties

try: #Restricts database to the domain
  for i in range(len(hw_trans)):
    if hw_trans[i,0] >= hw_min: #If finds a transition greater or equal to min domain
      trans_i = i #Saves index
      break #Finishes search
  for j in range(len(hw_trans)):
    if hw_trans[-j-1,0] <= hw_max:
      trans_f = len(hw_trans)-j
      break
  hw_trans = hw_trans[trans_i:trans_f] #Transitions of interest only
except: #If it cannot load the database it will warn the user
  messagebox.showerror('Transition energies database', 'The transition energies database
      ↪ was incorrectly loaded. The calculation will stop.')
  return #Returns nothing

out = minimize(lm_res, params, method = 'leastsq', args =(x, data,
counts_exp_err)) #Minimizes with LM algorithm
values = out.params.valuesdict()

for i in ions: #Assigns the csd dictionary with new values
  csd[i] = values['nq' + i]

spectrum_plot(*args) #Plots
return csd #Returns csd dictionary for the user to obtain in the CSD GUI
```

Chapter 4

Analysis of an x-ray spectrum

This chapter shows an analysis of an x-ray spectrum from Ar plasma, obtained with SIMPA's ECRIS detailed in Sec. 2.2 and 2.3. The goal is to obtain a realistic CSD by minimizing the χ^2 value of the simulated spectrum using the methodology and physical mechanisms described in Sec. 2.4.

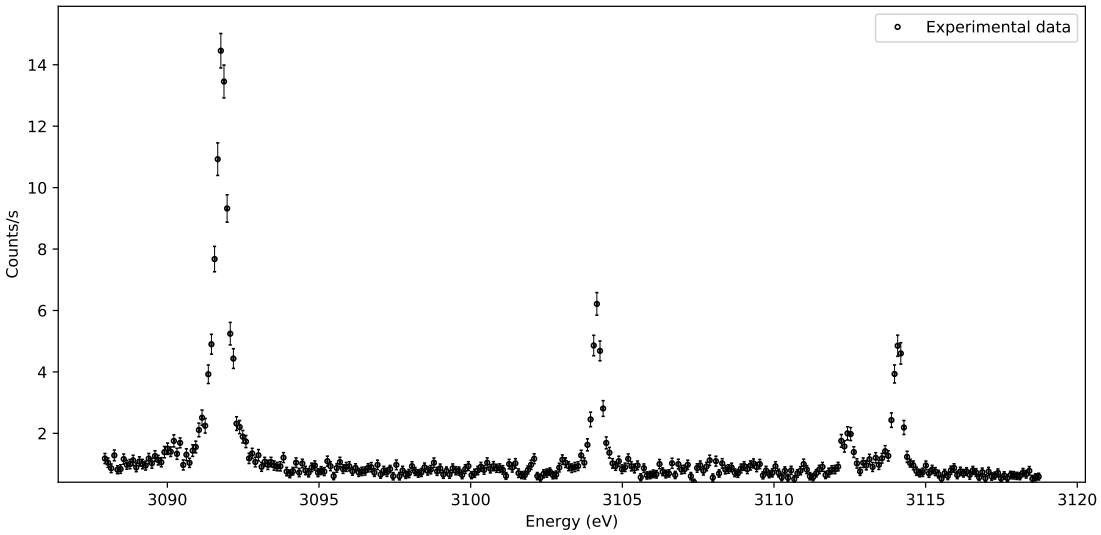

Figure 4.1: X-ray spectrum of Ar plasma taken with a DCS from SIMPA's ECRIS.

4.1 Transition energies

Fig. 4.1 shows the x-ray spectrum detected by the DCS of the ECRIS Ar plasma. The experimental energy values fall approximately in the $\sim [3087, 3119]$ eV range corresponding to strong emissions from the ions Ar^{14+}, Ar^{15+}, Ar^{16+}. Thus, from the transition database, out of 28 stored transitions, 18 are relevant to the energy region. Fig. 4.2 adds a stick plot with the x-ray lines in the database over the experimental data interval. An arbitrary CSD was initially given in order to get a simulated intensity for each transition, however, upon calculation, the main peaks easily emerged matching the ones in the experimental spectrum. The prominent peaks are attributed to the Be-like Ar ion $1s2s^2 2p\ ^1P_1 \rightarrow 1s^2 2s^2\ ^1S_0$ transition labeled as (1) in Fig. 4.2, the relativistic M1 transition $1s2s\ ^3S_1 \rightarrow 1s^2\ ^1S_0$ of the He-like Ar ion (2), and the doublet Li-like Ar ion $1s2s2p\ ^2P_{1/2,3/2} \rightarrow 1s^2 2s\ ^2S_{1/2}$ transition as (3).

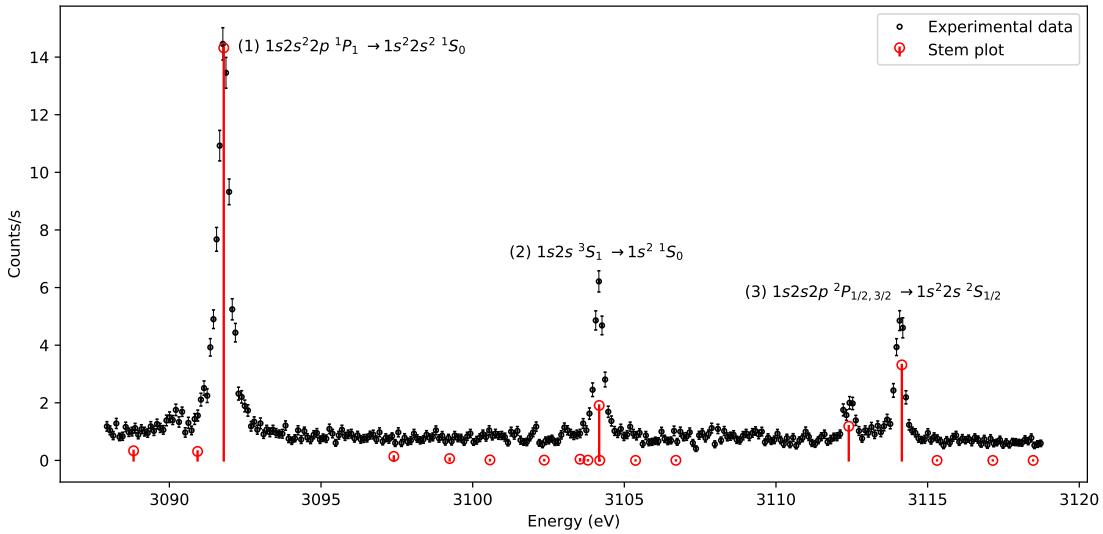

Figure 4.2: Stick plot in red showing the line intensities of an arbitrary CSD, showing the different transition energies considered in the experimental interval. Labeled (1) to (3) are the transitions in the database responsible for the most intense peaks in the experimental spectrum.

4.2 Pseudo-Voigt profile

A pseudo-Voigt distribution is applied to every x-ray line in Fig. 4.2, then added together for a single theoretical profile. The input parameters are the Gaussian/Lorentzian distribution fraction, and the Gaussian and Lorentzian FWHM values. With a CSD guess, these were determined in a first approach by trial and error and then the LM algorithm gave a better approximation.

The first step involved searching for the best fit pseudo-Voigt parameters for the transition lines labeled (1-3) in Fig. 4.2 separately. It is to expect, nonetheless, that the

experimental energy resolution of the DCS remains approximately equal in this range. Thus, the different values were averaged and adjusted once more, culminating in the guessed values in Tab. 4.1.

The LM algorithm on the pseudo-Voigt parameters was done separately to the main code as this spectrum brought some challenges to the fit. Since the peaks had few data points, an LM fit through the entire energy range resulted in wider than expected distributions due to the many background noise points with the peaks not matching in intensity with the experimental results. Consequently, the algorithm was applied after removing the data points outside the four main peaks. This caused the LM algorithm to return similar values consistently for different guesses. Even for far from optimal ones, the algorithm maintained a fraction between [56, 59]% and FWHM values for the Gaussian and Lorentzian distributions of ~ 0.62 eV and ~ 0.19 eV respectively. These energy values have physical meaning, as the dispersion on the Si 111 crystals broadens the x-ray line by an amount that is lower than 0.7 eV in this energy region [4]. The fraction between 56% and 59% showed no change to the overall χ^2_{red} value up to two decimal places, however, 56% was used since it resulted in a lower difference to the experimental intensity maxima.

Table 4.1: Table showing the pseudo-Voigt parameters after manually adjusting them ("Guess" column) and the results after applying the LM algorithm.

	Guess	**LM fit**
Voigt fraction (%)	36	56
Gaussian FWHM (eV)	0.60	0.62
Lorentzian FWHM (eV)	0.20	0.19

4.3 Charge-state distribution (CSD) guess

The Ar ions responsible for the detected emissions in the x-ray spectrum are Ar^{14+}, Ar^{15+}, and Ar^{16+}. Since the electron-impact ionization processes involve the removal of up to three electrons in the K and L shells, the distribution of the ions Ar^{11+}, Ar^{12+}, and Ar^{13+} must be considered as such processes can be responsible for the origin of the excited ionic configurations. Ergo, the input ions for the CSD range from Ar^{11+} up to Ar^{16+}.

4.3.1 Transfer function

The x-ray emission intensity detected in the DCS varies with the photon energy, meaning that an instrumental transfer function is necessary for a proper CSD analysis. The hyperbolic fit from Fig. 2.11 was added to the final spectrum resulting in the red line of Fig. 4.3. The initial CSD guess is shown in Tab. 4.2 after adjustments once the transfer function was loaded. Previous to this work, an extraction of the ion beam current was

performed in the same experimental conditions as the spectrum obtained (Fig. 4.1) [90]. The extraction is done on the plasma edges of SIMPA's ECRIS, resulting in a Gaussian like distribution from Ar^{11+} to Ar^{16+}. Although the plasma center behaves differently than the edges, it helps to estimate how the CSD should be. The CSD was inserted in the window shown in Fig. 3.6. The parameters from Fig. 3.7 were set in order to help minimize the χ^2 value. The "Min. χ^2" and normalization parameters were selected, with the normalization set to the relativistic M1 transition line of ~ 3104 eV.

Table 4.2: Table with the quantitative Ar ion CSD adjusted manually to the experimental spectrum after loading the transfer function. The theoretical spectrum is shown in Fig. 4.3.

Ar charge	**CSD (10^{16} ions/cm^3)**
11+	8
12+	4
13+	2
14+	1
15+	0.19
16+	0.021

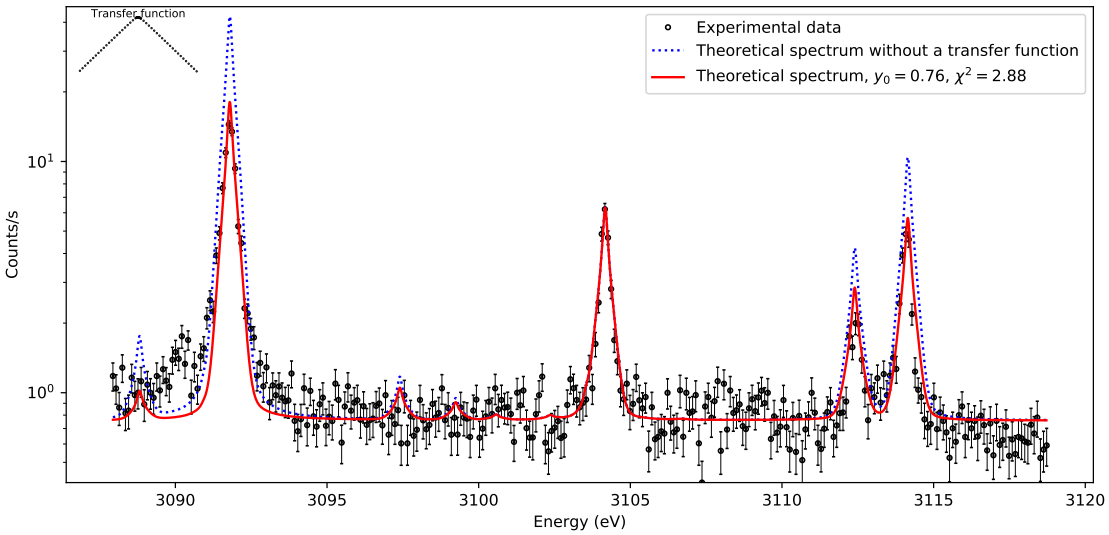

Figure 4.3: Logarithmic scale view of the calculated theoretical spectrum based on the CSD from Tab. 4.2 over the experimental data. The blue dotted line does not include the intensity transfer function shown in the top-left corner while the red line does. Both lines were normalized to the relativistic M1 transition line (~ 3104 eV). The background noise y_0 was calculated as the offset which results in the lowest χ^2 value.

4.3.2 Electron-impact phenomena contributions

Martins *et al* (2001) [47] showed an analysis of an Ar x-ray spectrum in an ECRIS plasma. The work covered a wider energy range starting with Ar ion charge 8+ up to 16+. The processes considered in the origin of excited states were electron-impact K-shell excitation and ionization only. Santos *et al* [49] provided a better analysis of many peaks by adding the consideration of double-KL and triple-KLL electron-impact ionization processes.

Fig. 4.4 shows how the different processes contribute to the final spectrum. From the electron-impact K-shell excitation theoretical profile, the relativistic M1 transition energy $1s2s\ ^3S_1 \rightarrow 1s^2\ ^1S_0$ is significantly below the experimental peak. Contrarily, the line with the addition of the K-shell ionization processes improve on the final result, approximating the experimental spectrum. The final addition of the double and triple ionization processes causes new small peaks to arise and generates final spectrum with a better fit. The new peaks and the growth of the main relativistic M1 line can be explained based on the balance equation 2.25. Even though the transition rate of the excited state $1s2s\ ^3S_1$ is a few orders of magnitude lower to other ions, this state is fed by all feeding mechanisms and more so from electron-impact K-shell ionization, justifying its intensity in the graph.

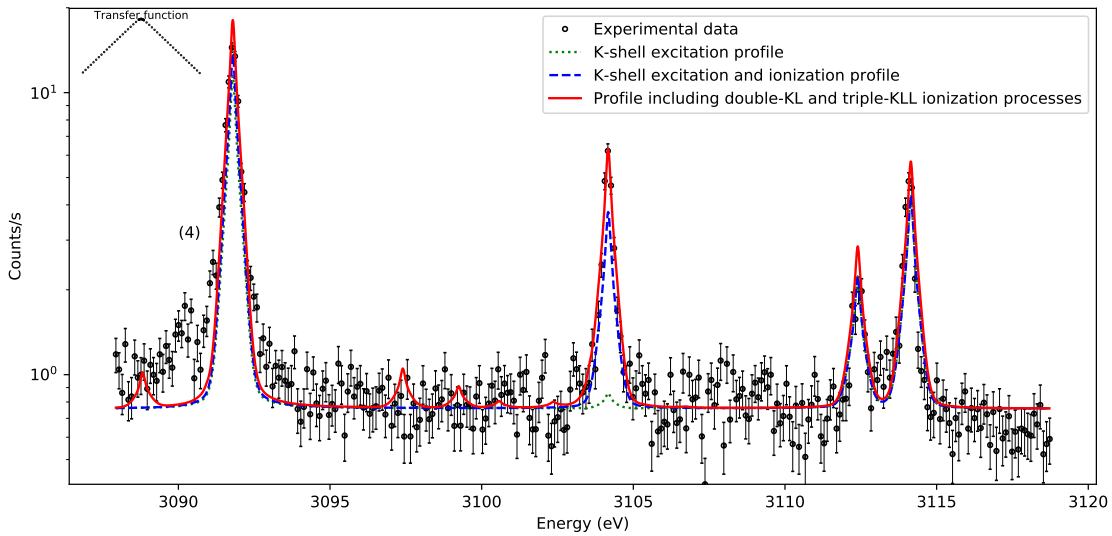

Figure 4.4: Graph with theoretical spectra under different considerations. The green dotted line shows a spectrum considering only K-shell excitation processes, the blue dashed line adds K-shell ionization processes to the previous line and the red line also includes double-KL and triple-KLL ionization processes. None of the processes managed to correspond to the observed bump by the left tail of the Be-like line or the peak in the labeled region (4).

4.3.3 Metastable states

Inside the ECRIS plasma, some ions in their excited states may not decay immediately. Their lifetime could be long enough to interact once more with the plasma electrons resulting in another excited state and a different decay energy. As seen in label (4) of Fig. 4.4, the experimental results show a peak at ~ 3090.2 eV which is not represented in the calculated spectrum. There are also other features, especially near the tails of the Be-like peak, that are not fully explained. In hindsight, considering the ions only in their fundamental state prior to excitation/ionization is not sufficient for a complete spectrum analysis. Hence, some metastable states may have to be considered.

Be-like Ar ion $1s^2 2s2p\ ^3P_0$ and B-like Ar ion $1s^2 2s2p^2\ ^2P_{3/2}$ may remain in the plasma long enough to justify their inclusion. However, the decay rate of the mentioned Be--like Ar ion configuration has been shown to be practically zero as their transitions only occur through hyperfine-induced or multiphoton interactions [91]. The B-like Ar ion $1s^2 2s2p^2\ ^2P_{3/2}$ has been measured to have a lifetime of 9.573(4)(5) ms(stat)(syst) [92], significantly lower than the collision frequency within the ECRIS [46], meaning their existence as an initial state must be considered.

Looking at the transition database in Tab. 3.1, the small bump by the Be-like peak (labeled (1) in Fig. 4.2) may stem from the decay of the excited state $1s2s2p^2\ ^1S_0$ to $1s^2 2s2p\ ^1P_1$ at an energy of 3090.93 eV. Since this transition is not shown in the final spectrum, it follows that the determined population of the excited state $1s2s2p^2$ is lacking the consideration of some long living metastable states from which it would originate. Thus, K-shell excitation and ionization processes from metastable states are added into the databases (see Tab. 3.2 and 3.3), resulting in the red lined spectrum of Fig. 4.5 and lowering the χ^2_{red} from 2.87 to 2.76. This consideration implies that some ground states are excited/ionized not to decay but to interact once more. Determining a CSD with a realistic metastable population is challenging as the ratio between the ground states that decay and that interact is unknown. Moreover, K-shell excitation and ionization are shown in Fig. 4.5 not to be enough to ensure the peak fit, meaning that double-KL and triple-KLL ionization processes may take relevant part. The problem arises as the cross section values for these phenomena are not yet well evaluated in the literature. Initially, it was thought that the peak around 3090.2 eV also stemmed from metastable states, however, unpublished studies by our group are pointing to the M2 Li-like Ar transition $1s2s2p\ ^4S_{5/2} \rightarrow 1s^2 2s\ ^2S_{1/2}$.

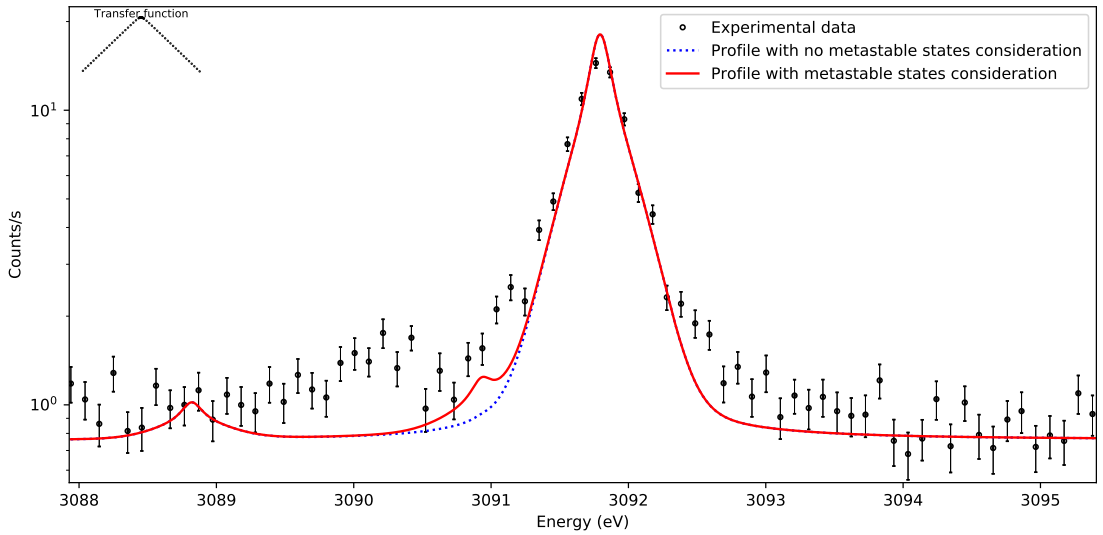

Figure 4.5: Graph of the spectrum zoomed in the region labeled as (4) in Fig. 4.4. The red line now includes metastable states which result in a bump by the main peak compared to the blue dotted line.

4.4 Levenberg-Marquardt (LM) algorithm results

Once a CSD guess is added to the window from Fig. 3.6, it is helpful to use the LM algorithm implemented into the code. Starting with a χ^2_{red} of 2.76 the aim was to reduce this value even more, while having a realistic CSD. The metastable states of Ar^{13+} and Ar^{14+} were not included in the algorithm (fixed to 1×10^{16} cm^{-3}) as their population are unknown.

At first, a random guess of the CSD was given to see how the LM would behave. The input values were restricted to a change of a factor of two for the first two fits, and then lifted on the third one. Tab. 4.3 shows the results of these steps. The code was quick to minimize the χ^2_{red} value to 2.55, however, the overlapping or lack of restrictions caused the algorithm to return a distribution which did not follow somewhat of a Gaussian profile with Ar^{13+} being more populated than Ar^{12+} for instance (see Ref. [90]). The ion Ar^{11+} was trending towards a less than expected value as well. This is due to the fact that the ion is considered only for the triple-KLL ionization process to the excited state of Ar^{14+} which has been shown to have low impact in the final spectrum (the minimization function is too flat to have an accurate result).

Table 4.3: Table with a random CSD input and the following LM fits done. The 2nd fit used the 1st fit distribution as the initial guess, with same logic for the 3rd one. The first two were restricted to a change by a factor of two whereas the third fit had no limits applied.

Charge	**Guess (10^{16} cm^{-3})**	**Fit 1 (10^{16} cm^{-3})**	**Fit 2 (10^{16} cm^{-3})**	**Fit 3 (10^{16} cm^{-3})**
11+	17	8.50	4.33	3.06
12+	13	6.50	3.31	5.83×10^{-5}
13+	6	3.00	5.41	2.46×10^{-4}
14+	3	1.50	1.06	1.63
15+	0.3	0.17	0.16	0.19
16+	0.01	0.02	0.04	0.22
χ^2_{red}	**4.43**	**3.58**	**2.55**	**2.54**

With these observations, a better strategy is to make use of the "LM fixed" column of Fig. 3.6 and attempt sensible readjustments through a few LM fits, reaching a realistic ion distribution. This was deemed better than programming restrictions as they caused extensive calculation times for these many variables. Tab. 4.4 shows in the first column the CSD guess from Tab. 4.2 and the following two columns corresponding to the first LM algorithm application and the final results after a few manual adjustments and some LM fits. As the calculated spectrum is normalized to the relativistic M1 transition line, the Ar^{16+} with the same transition energy, will be fixed for all fits at 0.021×10^{16} cm^{-3}. Once an appropriate CSD is given, the variables do not change as significantly as when given a random value. However, some results can either get stuck far from best fit or tend to drift away from a realistic ion distribution. Thus, after applying the LM algorithm with the CSD of Tab. 4.2, some changes were made to the CSD for more LM fits to avoid local minimums. This resulted in the final CSD from the third column of Tab. 4.4.

For some comparison, Adrouche's [90] extracted ion beam current determined the CSD in the ECRIS plasma edges. Tab. 4.5 shows the charge-state ratio to the ion Ar^{16+} for the theoretical spectrum and the ion current beam. Expectedly, the best fit results from the plasma center did not correspond entirely to the ion current beam. The biggest margin comes from the Ar^{12+} and Ar^{13+} with a difference of 25% and 30% to Adrouche's results. Notwithstanding, Ar^{14+} and Ar^{15+} ions resulted in really close values with less than 5% disparity. The proportion of Ar^{11+} did not significantly change the χ^2_{red} value as only triple-KLL ionization phenomena impacted the spectrum in this range, making estimation difficult, however a ratio of 323 to Ar^{16+} was reached, meaning a difference of 15% compared to the obtained ion beam current.

Table 4.4: Table with the manually obtained CSD as initial guess and the following LM fits applied. The second column shows the results obtained after using the LM algorithm once where the third is after some adjustments and a few LM fits for specific ions, preventing the CSD of drifting away from realistic values.

Charge	**Guess (10^{16} cm^{-3})**	**LM fit (10^{16} cm^{-3})**	**Adjusted CSD (10^{16} cm^{-3})**
11+	8	8.152	6.792
12+	4	4.291	4.377
13+	2	3.299	3.521
14+	1	1.238	0.853
15+	0.19	0.192	0.152
16+ (fixed)	0.021	0.021	0.021
χ^2_{red}	**2.76**	**2.71**	**2.59**

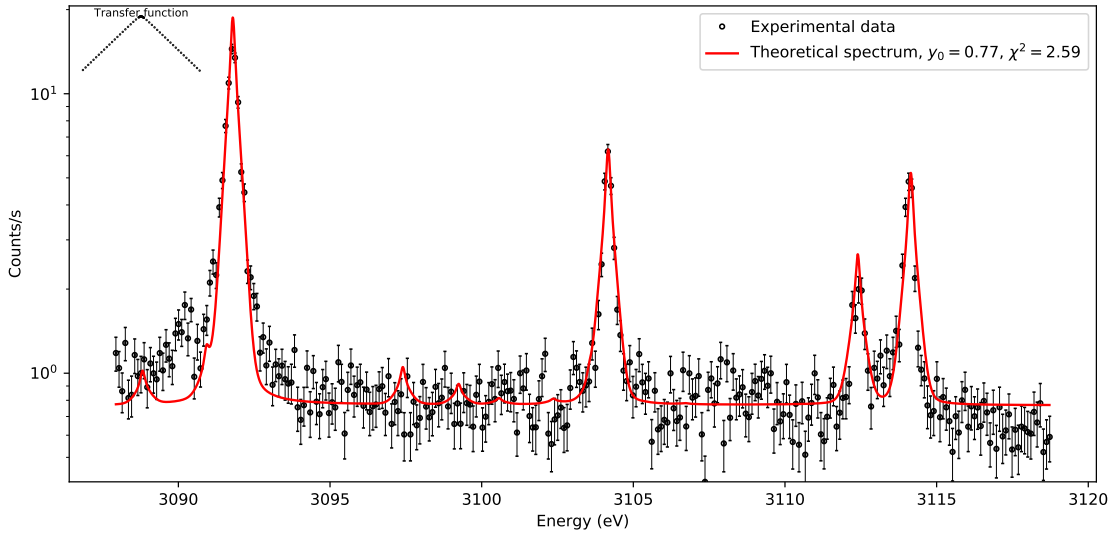

Figure 4.6: Spectrum with the CSD obtained from the LM algorithm.

Table 4.5: Table with the charge-state ratios obtained by the LM algorithm compared to [90] with extracted ion beam currents of the same ECRIS.

Ratio	**LM results**	**Adrouche [90]**	δ (%)
11+/16+	323	379	15
12+/16+	208	276	25
13+/16+	168	129	30
14+/16+	41	43	5
15+/16+	7	7	0

By making use of the available parameters in the code (Fig. 3.7) an even lower χ^2_{red} value can be achieved. With the "Two points" option, it is possible to add a slope to the offset as background noise. By iteratively clicking in different points of the spectrum, with the final CSD, the χ^2_{red} dropped from 2.59 to 2.14. Despite the short energy range, it is expected that the background noise does not remain constant due to the bremsstrahlung curve.

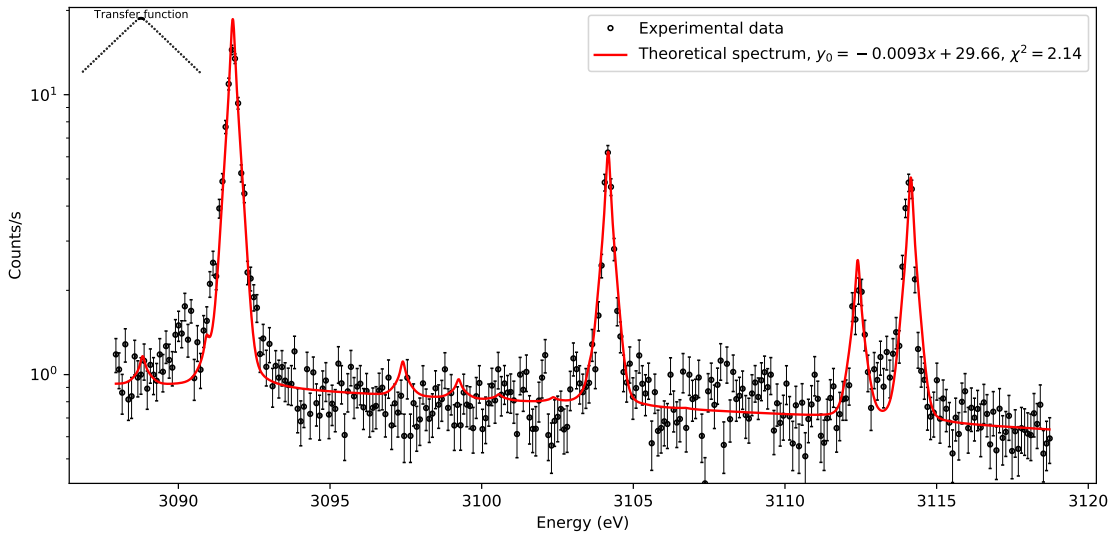

Figure 4.7: Final spectrum with the addition of a slope to the background noise by using the "Two points" parameter. After clicking in two different coordinates, a linear equation is given as offset for the background noise. With $y_0 = -0.0093x + 29.66$, the χ^2_{red} is equal to 2.14.

Chapter 5

Summary and final remarks

As the aim of this work, a Python code capable of estimating the CSD from x-ray spectra was developed for plasma diagnostics. With a database containing cross section values for electron-impact excitation and single, double, and triple ionization as well as transition energies and radiative yields, it is possible to simulate a spectrum by solving the balance equation 2.25 and the line intensity equation 2.26 for a given CSD.

5.1 Discussion of the results and conclusions

A highly resolved x-ray spectrum from a DCS of an ECRIS Ar plasma at SIMPA was provided for analysis. By collecting data of the Ar transition energies in the energy range of the experimental spectrum as well as cross sections for the considered processes, a fit of the theoretical spectrum over the experimental data was achieved. Firstly, the parameters from Fig. 3.7 were adjusted for the best fit. Separately to the main code, the experimental main peaks were taken for a manual adjustment of the pseudo-Voigt distribution shape followed by an improvement through the LM algorithm. This algorithm was implemented in the main code but as a mean to determine the best fit CSD. After adding the DCS's transfer function, a random CSD was given to understand how the method would behave. After processing the code twice, the LM is quick to minimize the χ^2 significantly, however, it would not follow the shape of the ion distribution from Adrouche's PhD thesis [90] and would be stuck on local minima. Note that although the extracted ion currents do not have to match exactly the ion distribution within the plasma, the overall shape of the distribution should not change drastically. An attempt to obtain a realistic CSD was performed by implementing restrictions on the CSD parameters, but this resulted in long computational time and most of the time causing a seemingly endless loop. Instead, a CSD was reached by iteratively changing the values and then applying

the LM algorithm close to the realistic minimum (similar to the reference distribution). After some adjustments and a final fit, a χ^2_{red} of 2.59 was achieved, improving from the manually obtained value of 2.79. Finally, a slope was added to the background offset, which resulted in the final χ^2_{red} of 2.14. The inclusion of double-KL and triple-KLL ionization processes was shown to be crucial for a more realistic analysis than Ref. [47]. It was shown that, although similar, the obtained CSD was not the same as Adrouche's. This is expected as the spectrum from the DCS represents the emissions in the plasma center, and the referenced distribution came from extracted ion beam currents from the edges.

A peak at $\sim$ 3090.2 eV was registered by the DCS, yet, not presented in the calculated spectrum. It was understood that considering only ground states to undergo electron-impact phenomena is insufficient regarding the plasma behavior. Some metastable states were added as they may live long enough to interact and result in excited states that were not yet considered. However, only databases for K-shell excitation and ionization were found, with no cross section values for double or triple ionization. Despite improving the fit, the new metastable states only managed to somewhat explain a small bump near the tail of the Be-like peak, as the missing values caused the theoretical line not match with the bump. Furthermore, this consideration implied that the excited states may not always result in a decay but in another interaction instead such as electronic and di-electronic recombinations. The ratio between states which decay and interact once again were unknown and not implemented in the code. This calls for a study of the metastable states inside the plasma in order to portray the whole picture in the spectrum. Afterwards, work done in our group concluded that the $\sim$ 3090.2 eV peak corresponds to the M2 Li-like Ar transition $1s2s2p\ ^4S_{5/2} \rightarrow 1s^2 2s\ ^2S_{1/2}$.

5.2 Future prospects

In the future, the developed code could add the LM algorithm to the pseudo-Voigt parameters and allow for changes for each peak individually. A more efficient way to compute the LM algorithm could be achieved by adding expressions and other restrictions to the CSD such as physical distributions based on thermal and non-thermal models. This could make only one fit necessary with less effort to estimate the CSD. Another avenue for subsequent work is to complete the code with other physical processes that were not considered in this work, such as electronic recombination, photoionization, two-photon emission, two-electron one-photon emission, hyperfine quenching and so on. This task could be aided with the CPIPES code [6] as it employs several plasma emission phenomena. The database directories are ready to be updated and expanded for a higher number of ions with different atomic structures and a greater range of energies. Calculations regarding the missing databases are needed and should be done with the state of the art MCDF method codes. With these, a wide variety of plasma diagnostics are possible in an ECRIS, at ITER or in astrophysical plasmas.

Bibliography

[1] L. F. Delgado-Aparicio. "Burning-plasma diagnostics: need for radiation-hardened detectors & electronics." *21st RD50 Workshop on Radiation hard semiconductor devices for very high luminosity colliders, CERN*. Nov. 2017.

[2] S. V. Mirnov. "Tokamak evolution and view to future." *Nuclear Fusion* 59.1 (Dec. 2018), p. 015001. ISSN: 0029-5515. DOI: 10.1088/1741-4326/aaee92.

[3] A. Donné. "Introduction to Plasma Diagnostics." *Fusion Science and Technology* 53.2T (Feb. 2008), pp. 379–386. DOI: 10.13182/fst08-a1723.

[4] M Guerra, P Amaro, C. I. Szabo, A Gumberidze, P Indelicato, and J. P. Santos. "Analysis of the charge state distribution in an ECRIS Ar plasma using high-resolution x-ray spectra." *Journal of Physics B: Atomic, Molecular and Optical Physics* 46.6 (Mar. 2013), p. 065701. DOI: 10.1088/0953-4075/46/6/065701.

[5] G. Douysset, H. Khodja, A. Girard, and J. P. Briand. "Highly charged ion densities and ion confinement properties in an electron-cyclotron-resonance ion source." *Phys. Rev. E* 61.3 (Mar. 2000), pp. 3015–3022. ISSN: 2470-0053. DOI: 10.1103/PhysRevE.61.3015.

[6] M. D. Avillez. "CPIPES - A software for the non-equilibrium ionisation evolution of the supernova and cosmic-rays driven ISM." *4th CRISM Conference*. 2018.

[7] M. A. de Avillez, G. J. Anela, and D. Breitschwerdt. "Variability of the adiabatic parameter in monoatomic thermal and non-thermal plasmas." *Astronomy & Astrophysics* 616 (Aug. 2018), A58. DOI: 10.1051/0004-6361/201832948.

[8] M. de Avillez, M. Guerra, J. P. Santos, and D. Breitschwerdt. "Relativistic electron impact ionization cross sections of carbon ions and application to an optically thin plasma." *Astronomy & Astrophysics* (Sept. 2019). DOI: 10.1051/0004-6361/201935337.

[9] R. Tong, Z. Chen, Z H. Jiang, X L. Zhang, Z Cheng, L Z. Liu, W Li, W Yan, Y N. Wei, Z F. Lin, Y Huang, and Z J. Yang. "Measurement of the toroidal radiation asymmetry during massive gas injection triggered disruptions on J-TEXT." *Review of Scientific Instruments* 89.10 (Oct. 2018), 10E113. DOI: 10.1063/1.5035187.

[10] A Murari, L Bertalot, G Bonheure, S Conroy, G Ericsson, V Kiptily, K Lawson, S Popovichev, M Tardocchi, V Afanasyiev, M Angelone, A Fasoli, J Källne, M Mironov, J Mlynar, D Testa, K. D. Zastrow, and J.-E. Contributors. "'Burning plasma' diagnostics for the physics of JET and ITER." *Plasma Physics and Controlled Fusion* 47.12B (Nov. 2005), B249–B262. DOI: 10.1088/0741-3335/47/12b/s19.

[11] P Beiersdorfer, J Clementson, J Dunn, M. F. Gu, K Morris, Y Podpaly, E Wang, M Bitter, R Feder, K. W. Hill, D Johnson, and R Barnsley. "The ITER core imaging x-ray spectrometer." *Journal of Physics B: Atomic, Molecular and Optical Physics* 43.14 (July 2010), p. 144008. DOI: 10.1088/0953-4075/43/14/144008.

[12] A. Shumack, J Rzadkiewicz, M. Chernyshova, K. Jakubowska, M. Scholz, A Byszuk, R Cieszewski, T. Czarski, W. Dominik, L Karpinski, G Kasprowicz, K. Pozniak, A. Wojenski, W. Zabolotny, N J. Conway, S Dalley, J. Figueiredo, T. Nakano, S Tyrrell, and V. Zoita. "X-ray crystal spectrometer upgrade for ITER-like wall experiments at JET." *Review of Scientific Instruments* 85.11 (Oct. 2014), 11E425. DOI: 10.1063/1.4891182.

[13] M. Polasik. "Theoretical multiconfiguration Dirac-Fock method study on the x-ray spectra of multiply ionized heavy atoms: The structure of the KLnlines." *Physical Review A* 39.2 (Jan. 1989), pp. 616–627. DOI: 10.1103/physreva.39.616.

[14] M. Polasik. "Theoretical simulation of the x-ray spectra of multiply ionized heavy atoms: The KLnspectra of molybdenum." *Physical Review A* 39.10 (May 1989), pp. 5092–5097. DOI: 10.1103/physreva.39.5092.

[15] K. Słabkowska, M. Polasik, E. Szymańska, J. Starosta, Ł. Syrocki, J. Rzadkiewicz, and N. R. Pereira. "Modeling of the L and M x-ray line structures for tungsten in high-temperature tokamak plasmas." *Physica Scripta* T161 (May 2014), p. 014015. DOI: 10.1088/0031-8949/2014/t161/014015.

[16] K Słabkowska, J Rzadkiewicz, Ł Syrocki, E Szymańska, A Shumack, M Polasik, N. R. Pereira, and J. contributors. "On the interpretation of high-resolution x-ray spectra from JET with an ITER-like wall." *Journal of Physics B: Atomic, Molecular and Optical Physics* 48.14 (May 2015), p. 144028. DOI: 10.1088/0953-4075/48/14/144028.

[17] Ł. Syrocki, E. Szymańska, K. Słabkowska, M. Polasik, and G. Pestka. "Modelling of the soft X-ray tungsten spectra expected to be registered by GEM detection system for WEST." *Nukleonika* 61.4 (Dec. 2016), pp. 433–436. ISSN: 0029-5922. DOI: 10.1515/nuka-2016-0071.

[18] K. Słabkowska, Ł. Syrocki, E. Węder, and M. Polasik. "Individual contributions of M X-ray line from Cu- and Co-like tungsten ions and L X-ray line from Ne-like molybdenum ions – Benchmarks for new approach to determine the high-temperature tokamak plasma parameters." *Nucl. Instrum. Methods Phys. Res., Sect. B* 408 (Oct. 2017), pp. 265–270. ISSN: 0168-583X. DOI: 10.1016/j.nimb.2017.05.051.

[19] Ł. Syrocki, K. Słabkowska, E. Węder, J. Starosta-Sztuczka, and M. Polasik. "Modeling of soft N, M and L X-ray lines from tungsten relevant to plasma parameters in the WEST tokamak." *Nuclear Instruments and Methods in Physics Research Section B: Beam Interactions with Materials and Atoms* 408 (Oct. 2017), pp. 257–264. DOI: 10.1016/j.nimb.2017.05.054.

[20] P. Beiersdorfer, J. Clementson, K. Widmann, M. Bitter, K. W. Hill, D. Johnson, R. Barnsley, H. K. Chung, and U. I. Safronova. "ITER core imaging X-ray spectroscopy: Atomic physics issues." *AIP Conference Proceedings* 1811.1 (Mar. 2017), p. 190001. ISSN: 0094-243X. DOI: 10.1063/1.4975744.

[21] J. Clementson and P. Beiersdorfer. "Atomic Data Of Tungsten For Current And Future Uses In Fusion And Plasma Science." *AIP Conference Proceedings* 1525 (2013), pp. 78–83. ISSN: 0094-243X. DOI: 10.1063/1.4802294.

[22] K P. Dere. "Ionization rate coefficients for the elements hydrogen through zinc." *Astronomy & Astrophysics* 466.2 (Feb. 2007), pp. 771–792. DOI: 10.1051/0004-6361:20066728.

[23] W. C. RONTGEN. "ON A NEW KIND OF RAYS." *Science* 3.59 (Feb. 1896), pp. 227–231. DOI: 10.1126/science.3.59.227.

[24] H. Moseley. "XCIII. The high-frequency spectra of the elements." *The London, Edinburgh, and Dublin Philosophical Magazine and Journal of Science* 26.156 (Dec. 1913), pp. 1024–1034. DOI: 10.1080/14786441308635052.

[25] A. A. Markowicz and R Van Grieken. "Handbook of X-ray Spectrometry." *Marcal Dekker, New York* (1993).

[26] I. Obodovskiy. "Nuclei and Nuclear Radiations." *Radiation*. Elsevier, 2019, pp. 41–62. DOI: 10.1016/b978-0-444-63979-0.00002-1.

[27] A. Sethi. "X-Rays: Interaction with Matter." *Encyclopedia of Medical Devices and Instrumentation* (Apr. 2006). DOI: 10.1002/0471732877.emd263.

[28] N. Itoh, M. Nakagawa, and Y. Kohyama. "Relativistic free-free opacity for a high-temperature stellar plasma." *The Astrophysical Journal* 294 (1985), p. 17. DOI: 10.1086/163269.

[29] E. P. Kontar, A. G. Emslie, A. M. Massone, M. Piana, J. C. Brown, and M. Prato. "Electron-Electron Bremsstrahlung Emission and the Inference of Electron Flux Spectra in Solar Flares." *The Astrophysical Journal* 670.1 (2007), pp. 857–861. DOI: 10.1086/521977.

[30] M. A. de Avillez and D. Breitschwerdt. "Non-relativistic Free–Free Emission due to then-distribution of Electrons—Radiative Cooling and Thermally Averaged and Total Gaunt Factors." *The Astrophysical Journal Supplement Series* 232.1 (Sept. 2017), p. 12. DOI: 10.3847/1538-4365/aa850a.

[31] P. Auger. "Sur l'effet photoélectrique composé." *Journal de Physique et le Radium* 6.6 (1925), pp. 205–208. DOI: 10.1051/jphysrad:0192500606020500.

[32] R. Tertian and F. Claisse. *Principles of Quantitative X-ray Fluorescence Analysis*. Heyden, 1982. ISBN: 0855017090.

[33] J Consolino, R Geller, and J Leroy. "1st Intern. Conf." *Ion Sources, Saclay* (1969), p. 537.

[34] H. Postma. "Multiply charged heavy ions produced by energetic plasmas." *Physics Letters A* 31.4 (Feb. 1970), pp. 196–197. DOI: 10.1016/0375-9601(70)90921-7.

[35] R. G.B.J.C. J. P. Apard S. Bliman. "2nd Intern. Conf." *Ion Sources, Wien* (1971), p. 632.

[36] G. Melin, F. Bourg, P. Briand, M. Delaunay, G. Gaudart, A. Girard, D. Hitz, J. P. Klein, P. Ludwig, T. K. Nguyen, M. Pontonnier, and Y. Su. "Status of development of ECR ion sources at Grenoble (invited)." *Review of Scientific Instruments* 65.4 (Apr. 1994), pp. 1051–1056. DOI: 10.1063/1.1145113.

[37] R Geller. "Electron cyclotron resonance sources: Historical review and future prospects." *Review of scientific instruments* 69.3 (1998), pp. 1302–1310.

[38] C. M. Lyneis and T. A. Antaya. "ERC sources for the production of highly charged ions." *Review of Scientific Instruments* 61.1 (Jan. 1990), pp. 221–224. DOI: 10.1063/1.1141881.

[39] R Geller. "ECRIS: The Electron Cyclotron Resonance Ion Sources." *Annual Review of Nuclear and Particle Science* 40.1 (Dec. 1990), pp. 15–44. DOI: 10.1146/annurev.ns.40.120190.000311.

[40] H. F. Beyer, H.-J. Kluge, and V. P. Shevelko. *X-Ray Radiation of Highly Charged Ions*. Springer Berlin Heidelberg, 1997. DOI: 10.1007/978-3-662-03495-8.

[41] J Arianer and R Geller. "The Advanced Positive Heavy Ion Sources." *Annual Review of Nuclear and Particle Science* 31.1 (Dec. 1981), pp. 19–51. DOI: 10.1146/annurev.ns.31.120181.000315.

[42] D. Leitner, C. Lyneis, S. Abbott, D. Collins, R. Dwinell, M. Galloway, M. Leitner, and D. Todd. "Next generation ECR ion sources: First results of the superconducting 28GHz ECRIS – VENUS." *Nuclear Instruments and Methods in Physics Research Section B: Beam Interactions with Materials and Atoms* 235.1-4 (2005), pp. 486–493. DOI: 10.1016/j.nimb.2005.03.230.

[43] S. Gammino, G. Ciavola, L. Celona, D. Hitz, A. Girard, and G. Melin. "Operation of the SERSE superconducting electron cyclotron resonance ion source at 28 GHz." *Review of Scientific Instruments* 72.11 (Nov. 2001), pp. 4090–4097. DOI: 10.1063/1.1405786.

[44] S. Biri, L. Simons, and D. Hitz. "Electron cyclotron resonance ion trap: A hybrid magnetic system with very high mirror ratio for highly charged ion production and trapping." *Review of Scientific Instruments* 71.2 (Feb. 2000), pp. 1116–1118. DOI: 10.1063/1.1150401.

[45] I. H. Hutchinson. *Principles of plasma diagnostics*. Vol. 44. 12. Cambridge University Press, Nov. 2002, p. 2603. DOI: 10.1017/cbo9780511613630.

[46] A. Gumberidze, M. Trassinelli, N. Adrouche, C. I. Szabo, P. Indelicato, F. Haranger, J.-M. Isac, E. Lamour, E.-O. Le Bigot, J. Merot, C. Prigent, J.-P. Rozet, and D. Vernhet. "Electronic temperatures, densities, and plasma x-ray emission of a 14.5 GHz electron-cyclotron resonance ion source." *Rev. Sci. Instrum.* 81.3 (Mar. 2010), p. 033303. ISSN: 0034-6748. DOI: 10.1063/1.3316805.

[47] M. C. Martins, A. M. Costa, J. P. Santos, P Indelicato, and F Parente. "Interpretation of x-ray spectra emitted by Ar ions in an electron-cyclotron resonance ion source." *Journal of Physics B: Atomic, Molecular and Optical Physics* 34.4 (Feb. 2001), pp. 533–543. DOI: 10.1088/0953-4075/34/4/303.

[48] P. M.D. G. Amaro. "Study of forbidden transitions in atomic systems." Doctoral dissertation. New University of Lisbon and University Pierre and Marie Currie, 2011.

[49] J. P. Santos, A. M. Costa, J. P. Marques, M. C. Martins, P. Indelicato, and F. Parente. "X-ray-spectroscopy analysis of electron-cyclotron-resonance ion-source plasmas." *Phys. Rev. A* 82.6 (Dec. 2010), p. 062516. ISSN: 2469-9934. DOI: 10.1103/PhysRevA.82.062516.

[50] Y.-K. Kim, K. Irikura, M. Rudd, M. Ali, P. S. J. Chang, J. Coursey, R. Dragoset, A. Kishore, K. Olsen, A. Sansonetti, G. Wiersma, D. Zucker, and M. Zucker. *Electron-Impact Cross Sections for Ionization and Excitation Database*. Aug. 1997. DOI: https://dx.doi.org/10.18434/T4KK5C.

[51] WIS Plasma Laboratory. *Databases for Atomic and Plasma Physics*. [accessed 31. Aug. 2019]. 2003. URL: http://plasma-gate.weizmann.ac.il/directories/databases.

[52] V. Fisher, V. Bernshtam, H. Golten, and Y. Maron. "Electron-impact excitation cross sections for allowed transitions in atoms." *Phys. Rev. A* 53.4 (Apr. 1996), pp. 2425–2432. ISSN: 2469-9934. DOI: 10.1103/PhysRevA.53.2425.

[53] H. van Regemorter. "Rate of Collisional Excitation in Stellar Atmospheres." *The Astrophysical Journal* 136 (Nov. 1962), p. 906. DOI: 10.1086/147445.

[54] J. P. Desclaux. "A multiconfiguration relativistic DIRAC-FOCK program." *Comput. Phys. Commun.* 9.1 (Jan. 1975), pp. 31–45. ISSN: 0010-4655. DOI: 10.1016/0010-4655(75)90054-5.

[55] P. Indelicato and J. P. Desclaux. "Multiconfiguration Dirac-Fock calculations of transition energies with QED corrections in three-electron ions." *Physical Review A* 42.9 (Nov. 1990), pp. 5139–5149. ISSN: 1050-2947. DOI: 10.1103/physreva.42.5139.

[56] P. Indelicato and J. P. Desclaux. *computer program MCDFGME, a multiconfiguration Dirac-Fock and general matrix elements program*. [accessed 31. Jan. 2019]. 2005. URL: http://dirac.spectro.jussieu.fr/mcdf.

[57] Y.-K. Kim and K.-t. Cheng. "Beth cross sections for the sodium isoelectronic sequence." *Phys. Rev. A* 18.1 (July 1978), pp. 36–47. ISSN: 2469-9934. DOI: 10.1103/PhysRevA.18.36.

[58] M. Rauscher, T. Salditt, and H. Spohn. "Small-angle x-ray scattering under grazing incidence: The cross section in the distorted-wave Born approximation." *Physical Review B* 52.23 (Dec. 1995), pp. 16855–16863. DOI: 10.1103/physrevb.52.16855.

[59] M. Dingfelder, S. Segui, and J. Fernández-Varea. "Distorted-wave ionization and x-ray production cross sections of the K shell of Cu and the L shells of Ag, In, and Sn by positron impact." *Physical Review A* 77.6 (June 2008). DOI: 10.1103/PhysRevA.77.062710.

[60] Y. Nagashima, F. Saito, Y. Itoh, A. Goto, and T. Hyodo. "Measurement of Cu K-shell and Ag L-shell ionization cross sections by low-energy positron impact." *Phys. Rev. Lett.* 92.22 (June 2004), p. 223201. ISSN: 0031-9007. DOI: 10.1103/PhysRevLett.92.223201.

[61] P. G. Burke and K. A. Berrington. *Atomic and molecular processes: an R-matrix approach*. CRC Press, 1993. ISBN: 0-7503-0199-6.

[62] I. Bray and A. T. Stelbovics. "The convergent close-coupling method for a Coulomb three-body problem." *Comput. Phys. Commun.* 85.1 (Jan. 1995), pp. 1–17. ISSN: 0010-4655. DOI: 10.1016/0010-4655(94)00134-N.

[63] Y.-K. Kim and M. E. Rudd. "Binary-encounter-dipole model for electron-impact ionization." *Phys. Rev. A* 50.5 (Nov. 1994), pp. 3954–3967. ISSN: 2469-9934. DOI: 10.1103/PhysRevA.50.3954.

[64] M. Guerra, F. Parente, P. Indelicato, and J. P. Santos. "Modified binary encounter Bethe model for electron-impact ionization." *Int. J. Mass Spectrom.* 313 (Mar. 2012), pp. 1–7. ISSN: 1387-3806. DOI: 10.1016/j.ijms.2011.12.003.

[65] M. Guerra, F Parente, and J Santos. "Electron impact ionization cross sections of several ionization stages of Kr, Ar and Fe." *International Journal of Mass Spectrometry* 348 (Aug. 2013), pp. 1–8. DOI: 10.1016/j.ijms.2013.02.011.

[66] M. Guerra, P. Amaro, J. Santos, and P. Indelicato. "Relativistic calculations of screening parameters and atomic radii of neutral atoms." *Atomic Data and Nuclear Data Tables* 117-118 (Sept. 2017), pp. 439–457. DOI: 10.1016/j.adt.2017.01.001.

[67] W. Lotz. "Electron-impact ionization cross-sections for atoms up to Z=108." *Zeitschrift für Physik A Hadrons and nuclei* 232.2 (Apr. 1970), pp. 101–107. ISSN: 0939-7922. DOI: 10.1007/BF01393132.

[68] D. Bote, F. Salvat, A. Jablonski, and C. J. Powell. "Cross sections for ionization of K, L and M shells of atoms by impact of electrons and positrons with energies up to 1 GeV: Analytical formulas." *Atomic Data and Nuclear Data Tables - AT DATA NUCL DATA TABLES* 95.6 (Nov. 2009), pp. 871–909. DOI: 10.1016/j.adt.2009.08.001.

[69] A. K. F. Haque, M. R. Talukder, M. Shahjahan, M. A. Uddin, A. K. Basak, and B. C. Saha. "An extended empirical formula for inner-shell ionization of atoms." *J. Phys. B: At. Mol. Opt. Phys.* 43.11 (May 2010), p. 115201. ISSN: 0953-4075. DOI: 10.1088/0953-4075/43/11/115201.

[70] K. Kiss, G. Kálmán, J. Pálinkás, and B. Schlenk. "Investigation of inner-shell ionization by electron impact in the 60–600 keV energy region." *Acta Physica Academiae Scientiarum Hungaricae* 50.1 (Jan. 1981), pp. 97–102. DOI: 10.1007/bf03157961.

[71] R. Hippler, I. McGregor, M. Aydinol, and H. Kleinpoppen. "Ionization of xenon *L* subshells by low-energy electron impact." *Phys. Rev. A* 23.4 (4 Apr. 1981), pp. 1730–1736. DOI: 10.1103/PhysRevA.23.1730.

[72] V. P. Shevelko and H. Tawara. "Semiempirical formulae for multiple ionization of neutral atoms and positive ions by electron impact." *J. Phys. B: At. Mol. Opt. Phys.* 28.18 (Sept. 1995), pp. L589–L594. ISSN: 0953-4075. DOI: 10.1088/0953-4075/28/18/004.

[73] C. Belenger, P. Defrance, E. Salzborn, V. Shevelko, H. Tawara, D. Uskov, and R. Author). "Double ionization of neutral atoms, positive and negative ions by electron impact." *JOURNAL OF PHYSICS B-ATOMIC MOLECULAR AND OPTICAL PHYSICS* 30.11 (June 1997), pp. 2667–2679. ISSN: 0953-4075. DOI: 10.1088/0953-4075/30/11/017.

[74] P. Indelicato. "Projection operators in multiconfiguration Dirac-Fock calculations: Application to the ground state of heliumlike ions." *Phys. Rev. A* 51.2 (Feb. 1995), pp. 1132–1145. ISSN: 2469-9934. DOI: 10.1103/PhysRevA.51.1132.

[75] I. P. Grant and H. M. Quiney. "Foundations of the Relativistic Theory of Atomic and Molecular Structure." *Advances in Atomic and Molecular Physics* 23 (Jan. 1988), pp. 37–86. ISSN: 0065-2199. DOI: 10.1016/S0065-2199(08)60105-0.

[76] C. Barué, M. Lamoureux, P. Briand, A. Girard, and G. Melin. "Investigation of hot electrons in electron-cyclotron-resonance ion sources." *J. Appl. Phys.* 76.5 (Sept. 1994), pp. 2662–2670. ISSN: 0021-8979. DOI: 10.1063/1.357563.

[77] R. Pras, M. Lamoureux, A. Girard, H. Khodja, G. Melin, and I. 97). "Electron cyclotron resonance ion source ionic currents (both in the stable and periodic regimes) modeled in relation with the hot electron temperature via the potential dip." *Rev. Sci. Instrum.* 69.2 (Feb. 1998), pp. 700–702. ISSN: 0034-6748. DOI: 10.1063/1.1148556.

[78] J. Kiusalaas. *Numerical Methods in Engineering with Python*. Cambridge University Press, 2005. ISBN: 978-0-521-85287-6.

[79] M. C. Martins, J. P. Marques, A. M. Costa, J. P. Santos, F. Parente, S. Schlesser, E.-O. Le Bigot, and P. Indelicato. "Production and decay of sulfur excited species in an electron-cyclotron-resonance ion-source plasma." *Phys. Rev. A* 80.3 (Sept. 2009). ISSN: 2469-9926. DOI: 10.1103/PhysRevA.80.032501.

[80] G. Melin. "Electron cyclotron resonance ion sources of highly charged ions: from classical to superconducting sources." *International Journal of Mass Spectrometry* 192.1-3 (Sept. 1999), pp. 87–97. DOI: 10.1016/s1387-3806(99)00129-3.

[81] A. COSTA, M. MARTINS, F PARENTE, J. SANTOS, and P INDELICATO. "DIRAC–FOCK TRANSITION ENERGIES AND RADIATIVE AND RADIATIONLESS TRANSITION PROBABILITIES FOR Ar9 TO Ar16 ION LEVELS WITH K-SHELL HOLES." *Atomic Data and Nuclear Data Tables* 79.2 (Nov. 2001), pp. 223–239. DOI: 10.1006/adnd.2001.0869.

[82] M. A. de Avillez and D. Breitschwerdt. "Temperature-averaged and total free-free Gaunt factors forand Maxwellian distributions of electrons." *Astronomy & Astrophysics* 580 (Aug. 2015), A124. DOI: 10.1051/0004-6361/201526104.

[83] P. H. Gavin. "The Levenberg-Marquardt algorithm for nonlinear least squares curve-fitting problems: Department of Civil and Environmental Engineering." *Duke University* 10.1 (2019).

[84] O. Nelles. *Nonlinear System Identification*. Springer Berlin Heidelberg, 2001. ISBN: 978-3-642-08674-8. DOI: 10.1007/978-3-662-04323-3.

[85] M. K. Transtrum, J. P. Sethna, M. K. Transtrum, and J. P. Sethna. "Improvements to the Levenberg-Marquardt algorithm for nonlinear least-squares minimization." *arXiv preprint arXiv:1201.5885* (Jan. 27, 2012). arXiv: 1201.5885v1 [physics.data-an].

[86] J. J. Waterfall, F. P. Casey, R. N. Gutenkunst, K. S. Brown, C. R. Myers, P. W. Brouwer, V. Elser, and J. P. Sethna. "Sloppy-Model Universality Class and the Vandermonde Matrix." *Phys. Rev. Lett.* 97 (15 Oct. 2006), p. 150601. DOI: 10.1103/PhysRevLett.97.150601.

[87] R. N. Gutenkunst, J. J. Waterfall, F. P. Casey, K. S. Brown, C. R. Myers, and J. P. Sethna. "Universally Sloppy Parameter Sensitivities in Systems Biology Models." *PLoS Computational Biology* 3.10 (Oct. 2007), e189. DOI: 10.1371/journal.pcbi.0030189.

[88] R. Li, A. Reynolds, and D. Oliver. "History Matching of Three-Phase Flow Production Data." *SPE Journal* 8.04 (Dec. 2003), pp. 328–340. DOI: doi.org/10.2118/87336-PA.

[89] M. Newville, T. Stensitzki, D. B. Allen, and A. Ingargiola. *LMFIT: Non-Linear Least-Square Minimization and Curve-Fitting for Python*. 2014. DOI: 10.5281/zenodo.11813.

[90] N. Adrouche. "Diagnostic du plasma de la source dions ECR SIMPA par spectroscopie." Theses. Université Pierre et Marie Curie - Paris VI, Sept. 2006. URL: https://tel.archives-ouvertes.fr/tel-00105774.

[91] R. W. Schmieder. "Double- and Triple-Photon Decay of Metastable $^3P_0$ Atomic States." *Phys. Rev. A* 7 (5 May 1973), pp. 1458–1468. DOI: 10.1103/PhysRevA.7.1458.

[92] A. Lapierre, U. D. Jentschura, J. R. Crespo López-Urrutia, J. Braun, G. Brenner, H. Bruhns, D. Fischer, A. J. González Martínez, Z. Harman, W. R. Johnson, C. H. Keitel, V. Mironov, C. J. Osborne, G. Sikler, R. Soria Orts, V. Shabaev, H. Tawara, I. I. Tupitsyn, J. Ullrich, and A. Volotka. "Relativistic Electron Correlation, Quantum Electrodynamics, and the Lifetime of the $1s^2 2s^2 2p\ ^2P^o_{3/2}$ Level in Boronlike Argon." *Phys. Rev. Lett.* 95 (18 Oct. 2005), p. 183001. DOI: 10.1103/PhysRevLett.95.183001.

Appendix A

Submitted poster

Between the 13th and the 17th of May 2019, this work was presented during a poster session for the spring school and workshop by EXSA Quantitative Methods in X-Ray Spectrometry in Caparica, Portugal.

Quantification of x-ray spectra from highly charged ions plasmas for astrophysical and energy applications

A. Fernandes[1], J. P. Santos[1], M. de Avillez[2], M. Guerra[1]

[1]Department of Physics, Faculty of Sciences and Technology, New University of Lisbon, 2829-516 Caparica, Portugal
[2]Department of Mathematics, University of Évora, R. Romão Ramalho 59, 7000 Évora, Portugal

Abstract

Plasma diagnostics are crucial in astrophysics and for projects like ITER. These diagnostics demand theoretical studies in order to understand the origin of spectral emission observed in the plasma. From the balance between the creation and decay of excited states, one can infer on the abundance of the ions within the plasma. Thus, electron impact ionization and excitation, which require cross section values for any creation process, need to be evaluated for a large number of states and for a wide energy range. Typically, the values are determined computationally with models such as the DWBA and MRBEB, due to the simplicity of the approach. With these, and the line intensities of the spectrum, it is possible to determine the charge state distribution within the plasma. With the ion structure information, we can determine, for example, the ion temperature and impurities from wall contamination in the plasma.

Method

For a proper x-ray spectrum analysis, with the aim of estimating the ion charge state density (CSD), one must take into consideration the physical processes in the plasma. The methodology for the CSD estimation used by Santos *et al.* [1] goes as follows:

1. The spectrum of characteristic x-rays from ions inside the plasma is measured;
2. The excited states that produce the x-ray spectrum are identified through extensive atomic databases;
3. The main processes leading to these excited states, from the ground configurations, are found and the corresponding cross sections are calculated, using a physically justified electron distribution function;
4. Radiative and radiationless transition energies and probabilities are calculated for the identified excited states;
5. From the comparison of the peak intensities in theoretical and experimental spectra, with a Levenberg-Marquardt algorithm, the CSD is obtained;

The phenomena considered in this work are electron impact excitation, single, double and triple ionization, transition energies and probabilities, and the distribution of electron energies in the plasma. It should be noted that processes such as dielectronic recombination, charge exchange, and radiative recombination rates, albeit present, are of low influence to the plasma presented in comparison [2].

The balance equation is given as follows:

$$N_0^q \langle N_e v \sigma_i^{K-exc,q} \rangle + N_0^{q-1} \langle N_e v \sigma_i^{K-ion,(q-1,q)} \rangle + \\ + N_0^{q-2} \langle N_e v \sigma_i^{K-ion,(q-2,q)} \rangle + N_0^{q-3} \langle N_e v \sigma_i^{K-ion,(q-3,q)} \rangle \\ = N_i^{K,q} A_i^q$$

It takes into account the charge state density $N_i^{K,q}$, the radiative or radiationless decay probability A_{ij}^q and the rate of the processes $N_0^q \langle N_e v \sigma_i^{process} \rangle$. For an energy $\hbar\omega$, the line intensities are calculated with:

$$I_{ij}^q = \hbar\omega A_{ij}^q N_i^{K,q}$$

Ar spectrum analysis

Program database

The spectrum analysis is based on two sets of databases. One regarding the states leading to a certain excited state and another the decay. The former was considered to be in its ground state, however, two metastable states were present long enough to decay through a radiative transition.

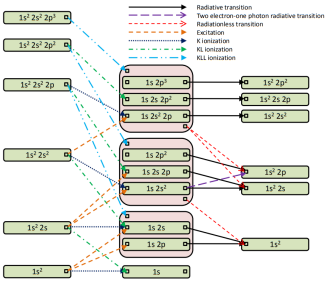

The program searches the transition database of the given spectrum range and calculates the line intensities considering the various processes' cross section database. The line intensities require adjustments in the balance equation, done by trial and error or by fitting using a Levenberg-Marquardt algorithm to give a sense of the charge state density in the plasma. Finally, a linear combination of a Lorentzian and a Gaussian distribution is made in order to have an adjustable Voigt profile.

Results

The following graph shows the spectrum with a transition range obtained from Ref. [2]. The 28 transitions provide a profile which gets closer to the experimental data as it considers more processes responsible for the excited state.

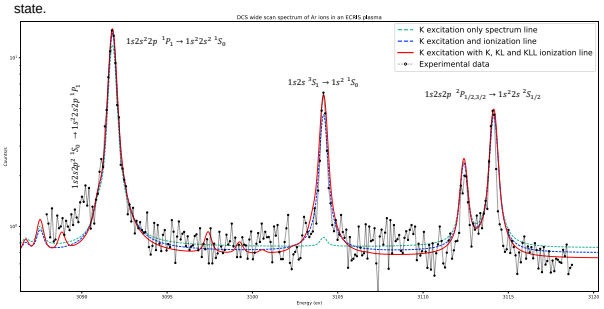

It is to note that for the transition $1s2s\ ^3S_1 \rightarrow 1s^2\ ^1S_0$, the K-shell excitation process leading to the excited state $1s2s$ is not enough for a proper spectrum line and that the ionization processes must be considered.

The determined charge-state density relative to the Ar^{16+} was compared to ionic currents from Adrouche [3].

CS ratio	Determined	Adrouche
$11^+/16^+$	400	379
$12^+/16^+$	200	276
$13^+/16^+$	100	129
$14^+/16^+$	50	43
$15^+/16^+$	10	7

Conclusion

A program is being made with databases capable of quantifying x-ray spectra from highly charged ions. The radiative decay transitions are not enough for a proper experimental plasma diagnosis, therefore, a cross section database is used to determine the predominance of certain excited states based on ground states and some significant metastable states. The database includes electron impact excitation, single, double and triple ionization. For an even improved approach, the code will take into account processes such as dielectronic recombination, charge exchange, and radiative recombination rates, with the help of programs such as CPIPES.

References

[1] Santos J P, Costa A M, Marques J P, Martins M C, Indelicato P and Parente F 2010 Phys. Rev. A 82 062516
[2] Costa A M, Martins M C, Parente F, Santos J P and Indelicato P 2001 Atomic Data and Nuclear Data Tables 79 223–239
[3] Adrouche N 2006 Diagnostic du plasma de la source d'ions ECR SIMPA par spectroscopie X PhD Thesis Université Paris VI Pierre et Marie Curie

FACULDADE DE CIÊNCIAS E TECNOLOGIA UNIVERSIDADE NOVA DE LISBOA
LIBPhys-UNL
FCT Fundação para a Ciência e a Tecnologia
MINISTÉRIO DA CIÊNCIA, TECNOLOGIA E ENSINO SUPERIOR

Figure A.1: Submitted poster presented at the EXSA Quantitative Methods in X-Ray Spectrometry 2019.